

TRIANGULUM-ANDROMEDA OVERDENSITY: A REGION WITH A COMPLEX STELLAR POPULATION

J. V. SALES SILVA¹, H. D. PEROTTONI^{2,3}, K. CUNHA^{1,5}, H. J. ROCHA-PINTO², F. ALMEIDA-FERNANDES^{2,3}, DIOGO SOUTO¹, S. R. MAJEWSKI⁶

(Received July 31, 2019; Revised August; Accepted August)
Draft version October 22, 2019

ABSTRACT

The Triangulum–Andromeda (TriAnd) overdensity is a distant structure of the Milky Way located in the second Galactic quadrant well below the Galactic plane. Since its discovery, its nature has been under discussion, whether it could be old perturbations of the Galactic disk or the remains of a disrupted former dwarf galaxy. In this study, we investigate the kinematics and chemical composition in 13 stars selected as TriAnd candidates from 2MASS photometry. The sample was observed using the GRACES high-resolution spectrograph attached to the Gemini North telescope. Based on radial velocities obtained from the spectra and the astrometric data from GAIA, three different kinematic criteria were used to classify our sample stars as belonging to the TriAnd overdensity. The TriAnd confirmed members in our sample span a range in metallicities, including two metal-poor stars ($[\text{Fe}/\text{H}] \sim -1.3$ dex). We show that the adopted kinematical classification also chemically segregates TriAnd and non-TriAnd members of our sample, indicating a unique chemical pattern of the TriAnd stars. Our results indicate different chemical patterns for the $[\text{Na}/\text{Fe}]$, $[\text{Al}/\text{Fe}]$, $[\text{Ba}/\text{Fe}]$, and $[\text{Eu}/\text{Fe}]$ ratios in the TriAnd stars when compared to the chemical pattern of the local disk; the paucity of studies chemically characterizing the outer disk population of the Milky Way is the main obstacle in establishing that the TriAnd population is chemically similar to field stars in the outer disk. But TriAnd chemical pattern is reminiscent of that found in outer disk open clusters, although the latter are significantly more metal-rich than TriAnd.

Subject headings: Galaxy: disk — stars: abundances — stars: kinematic

1. INTRODUCTION

In the last decades, the level of detail and detection of structure in the Galaxy has intensified considerably with the advance of the observational power of the telescopes and their instruments, and the completion of large surveys, which enables the discoveries of dwarf galaxies (Willman et al. 2005; Belokurov et al. 2007; Drlica-Wagner et al. 2015; Koposov et al. 2015; Laevens et al. 2015; Kim & Jerjen 2015), stellar streams (e.g., Newberg et al. 2002; Majewski et al. 2003; Grillmair 2006; Bernard et al. 2016; Malhan et al. 2018; Shipp et al. 2018; Perottoni et al. 2019), and stellar overdensities (e.g., Rocha-Pinto et al. 2004; Majewski et al. 2004; Martin et al. 2007; Jurić et al. 2008; Belokurov et al. 2007; Sesar et al. 2007; Watkins et al. 2009; Li et al. 2016). One of these overdensities is Triangulum–Andromeda (TriAnd), which was discovered by Rocha-Pinto et al. (2004) and Majewski et al. (2004). Rocha-Pinto et al. (2004) found TriAnd from a sample of 2MASS M giant candidates while searching for asymmetries in the sky-projected stellar density, and Majewski et al. (2004) located the main-sequence and the main-sequence turnoff of the TriAnd

overdensity using data from a deep photometric survey developed to study the stellar halo of M 31.

The TriAnd overdensity is very tenuous and extends to approximately 1000 square degrees covering $100^\circ < l < 150^\circ$ and $-15^\circ > b > -35^\circ$ (Rocha-Pinto et al. 2004; Deason et al. 2014; Sheffield et al. 2014; Perottoni et al. 2018), in the southern Galactic hemisphere. Estimates for the heliocentric distance of the TriAnd population range between 15–21 kpc (Sheffield et al. 2014; Martin et al. 2014), its age spans a range between 6–10 Gyr (Sheffield et al. 2014) and it has stars that go ~ 7 kpc below the galactic plane (Hayes et al. 2018). Moreover, the TriAnd stellar population seems to move in orbits nearly coplanar to the disk with a low velocity dispersion (Rocha-Pinto et al. 2004; Sheffield et al. 2014) and it is possibly associated with Mon/GASS and A13 in the velocity space (Li et al. 2017; Sheffield et al. 2018).

As other overdensities seen at low b , TriAnd is subject to many hypotheses that suggest it to be part of the outer Galactic disk (Xu et al. 2015; Price-Whelan et al. 2015; Li et al. 2017; Sheffield et al. 2018; Hayes et al. 2018; Bergemann et al. 2018) or of a disrupted dwarf galaxy (Chou et al. 2011; Sheffield et al. 2014; Deason et al. 2014). The ratio of RR Lyrae stars to M giant stars in the TriAnd region is compatible with that of the Galactic disk and not with the typical ratio for a dwarf galaxy (Price-Whelan et al. 2015). But this could be a consequence of its metallicity, for TriAnd stellar population is more metal-rich than that of known dwarf galaxies — present TriAnd $[\text{Fe}/\text{H}]$ estimates range from -0.4 to -1.3 dex (Deason et al. 2014; Sheffield et al. 2014; Hayes et al. 2018; Bergemann et al. 2018; Fernández-Alvar et al. 2019).

¹ Observatório Nacional/MCTIC, R. Gen. José Cristino, 77, 20921-400, Rio de Janeiro, Brazil

² Universidade Federal do Rio de Janeiro, Observatório do Valongo, Lad. Pedro Antônio 43, 20080-090, Rio de Janeiro, Brazil

³ Departamento de Astronomia, IAG, Universidade de São Paulo, Rua do Matão, 1226, 05509-900, São Paulo, Brazil

⁴ Steward Observatory, University of Arizona Tucson AZ 85719

⁵ Departamento de Física, Universidade Federal de Sergipe, Av. Marechal Rondon, S/N, 49000-000 São Cristóvão, SE, Brazil

⁶ Department of Astronomy, University of Virginia, Charlottesville, VA 22904-4325, USA

Chou et al. (2011) performed the first high-resolution study of six stars belonging to TriAnd. They obtained that three of their targets had $[\text{Ti}/\text{Fe}]$ in agreement with the disk pattern, while for three others their $[\text{Ti}/\text{Fe}]$ was lower than the disk value; they concluded that TriAnd could have an extragalactic origin. More recently, Bergemann et al. (2018) and Hayes et al. (2018) using optical and infrared high-resolution spectroscopy, respectively, found support for a Galactic origin for the TriAnd stars, despite their large height below the Galactic plane (≈ 7 kpc, Hayes et al. 2018). Both studies attributed their odd location to tidal interactions of the disk with passing or merging dwarf galaxies. This hypothesis is corroborated by several theoretical works on N-Body and hydrodynamical simulations (Purcell et al. 2011; Gómez et al. 2013, 2016; Laporte et al. 2018a,b).

Bergemann et al. (2018) presented chemical abundances of O, Na, Mg, Ti, Fe, Ba, and Eu, finding that TriAnd stars have an abundance pattern similar to that of Galactic disk stars, while Hayes et al. (2018), using chemical abundances results from the APOGEE survey from DR14 (Majewski et al. 2017) for Fe, C, N, Mg, K, Ca, Mn and Ni concluded that TriAnd stars are similar to outer disk stars, but with a metallicity ($[\text{Fe}/\text{H}] \approx -0.8$ dex) lower than most of those with $R_{GC} < 15$ kpc.

Considering the interest in further understanding the nature of the TriAnd overdensity, in this study we conduct a kinematic and chemical study of a sample of thirteen TriAnd candidate stars observed with high-resolution spectroscopy to investigate their chemokinematical properties. We determined the chemical abundances of seven elements (Na, Al, Fe, Cr, Ni, Ba and Eu) for all the stars in our sample; moreover, using astrometric data from Gaia, we derived the kinematic properties and orbits of the stars.

2. SAMPLE SELECTION AND OBSERVATIONS

A TriAnd candidate star sample was initially defined by Rocha-Pinto et al. (2004) from the 2MASS catalog (Cutri et al. 2003) through a color criterion in the $J-H$ vs. $J-K$ diagram that segregates M giants from M dwarfs. It was the same criterion employed by Majewski et al. (2003) and Rocha-Pinto et al. (2003) for mapping the Sagittarius dSph tidal tails and the Monoceros stream, respectively. Rocha-Pinto et al. (2004) used a statistical method to estimate the most likely distance of each star, such that the TriAnd candidate sample was formed by those M giants having $100^\circ < l < 150^\circ$, $-50^\circ < b < -15^\circ$ and most likely distances between 15 and 30 kpc from the Sun⁷.

We overimposed this M giant TriAnd sample to the TriAnd map made by Perottoni et al. (2018), which is based on SDSS main-sequence stars, to randomly select our spectroscopic program stars. These were picked around the coordinates of three of the densest regions in the Perottoni et al.'s map since our goal was to study whether there were chemical differences between those three regions. The final sample selected for the spectroscopic program according to color-magnitude selection areas from Sheffield et al. (2014) is likely to be formed

⁷ Recently, Sheffield et al. (2014) showed that Rocha-Pinto et al.'s selection included stars from both TriAnd and TriAnd2, which was discovered a few years later by Martin et al. (2007).

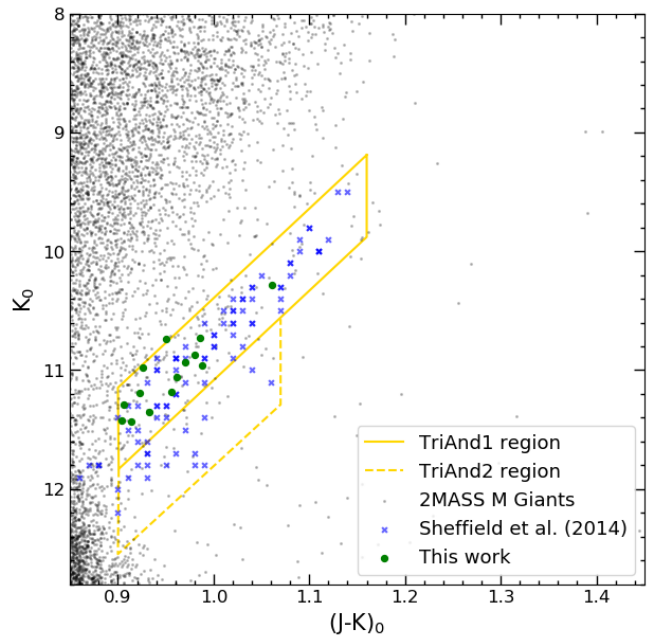


FIG. 1.— Color-magnitude diagram of 2MASS M giants candidates located between $90^\circ < l < 160^\circ$ and $-10^\circ > b > -40^\circ$. The green circles show the TriAnd candidates analysed in this work. The blue crosses show the TriAnd1 and TriAnd2 M giants candidates sample from Sheffield et al. (2014). The yellow parallelograms having the solid and dashed borders are, respectively, approximate selection regions for TriAnd1 and TriAnd2 members by Sheffield et al. (2014).

by a mix of TriAnd stars (see Figure 1) and a few interloping halo giants that may lay in the line of sight. We deredden the data the 2MASS following the Equations (1) from Majewski et al. (2003).

The observations of thirteen TriAnd candidate stars were carried out in the second half of 2016 (two exposures for each star) using the GRACES (Gemini Remote Access to CFHT ESPaDOnS Spectrograph) instrument (Tollestrup et al. 2012) attached to the Gemini North telescope located in Hawaii/USA. The data were reduced using the OPERA pipeline (Martioli et al. 2012) and included: bias subtraction, flat-field correction, and wavelength calibration; we used the IRAF package to perform spectra normalization. Our spectra have high-resolution ($R = 40,000$) and a $S/N \sim 50-70$ per \AA at 6000\AA . We determined the radial velocities of our sample using the task `fxcor` in IRAF to cross-correlate the observed spectra with templates from Munari et al. (2005). In Table 1 we show relevant information about the observed stars: star 2MASS identification, equatorial and galactic coordinates, J , H , K , $J-K$ magnitudes from 2MASS. In addition, we obtained from the ESO Archive the spectrum of the star 2M23174139+3113043 of the sample of Bergemann et al. (2018). This star was observed in the Very Large Telescope using the UVES spectrograph. For detailed information about this spectrum see Bergemann et al. (2018). We added this star to our sample for a comparison between the results in the two studies.

3. ATMOSPHERIC PARAMETERS AND ABUNDANCE ANALYSIS

TABLE 1
TRIAND CANDIDATES OBSERVED WITH GRACES.

2MASS ID	RA	DEC	l	b	J	H	K	K_0	$(J - K)_0$	
#	hh:mm:ss	dd:mm:ss	degree	degree	mag	mag	mag	mag		
1	00075751+3359414	00:07:57.510	33:59:41.400	112.731	-28.014	12.352	11.556	11.420	11.405	0.904
2	00534976+4626089	00:53:49.760	46:26:08.900	123.362	-16.434	11.914	11.032	10.867	10.833	0.980
3	00594094+4614332	00:59:40.940	46:14:33.200	124.419	-16.605	12.203	11.381	11.183	11.149	0.956
4	01020943+4643251	01:02:09.430	46:43:25.100	124.844	-16.108	12.268	11.480	11.292	11.256	0.906
5	01151944+4713512	01:15:19.440	47:13:51.200	127.135	-15.446	12.165	11.337	11.190	11.163	0.923
6	02485891+4312154	02:48:58.910	43:12:15.400	144.630	-14.660	11.398	10.506	10.284	10.256	1.061
7	23535441+3449575	23:53:54.410	34:49:57.500	109.755	-26.563	11.944	11.152	10.975	10.953	0.926
8	23481637+3129372	23:48:16.370	31:29:37.200	107.473	-29.475	12.080	11.274	11.059	11.028	0.961
9	02350813+4455263	02:35:08.130	44:55:26.300	141.550	-14.166	12.403	11.674	11.435	11.407	0.914
10	23495808+3445569	23:49:58.080	34:45:56.900	108.863	-26.421	11.744	10.896	10.729	10.714	0.86
11	02510349+4342045	02:51:03.490	43:42:04.500	144.743	-14.046	11.999	11.117	10.957	10.929	0.987
12	02475442+4429269	02:47:54.420	44:29:26.900	143.856	-13.597	11.972	11.105	10.931	10.895	0.971
13	02463235+4314481	02:46:32.350	43:14:48.200	144.199	-14.821	12.335	11.556	11.351	11.324	0.932
14	23174139+3113043 ^a	23:17:41.390	31:13:04.300	100.379	-27.515	11.750	10.920	10.740	10.701	0.950

Notes. Columns, from left to right: star 2MASS identification, R.A., decl., galactic coordinates (l and b), J , H , K , $J - K$ from 2MASS, K_0 , $(J - K)_0$.

^a Spectrum from ESO-ARCHIVE.

The first step was to define the line list and the model atmospheres that will be used to determine the chemical abundances and the atmospheric parameters of the stars in our sample.

Our list of Fe I and Fe II absorption lines is composed of about 170 lines, with the atomic parameters obtained from Heiter et al. (2015). To analyze the neutral and ionized Fe lines, we carefully looked whether the lines overlapped with other absorption features; thus only the unblended Fe absorption lines were used in our analysis. We measured the equivalent widths of the lines of the elements Fe, Na, Al, Cr and Ni using the task `splot` in IRAF. We note, however, that due to overlapping absorption lines it was not possible to determine chromium abundances for the entire sample. In the Appendix, we show the measurements of equivalent widths used to obtain chemical abundances. For the neutron capture elements (Ba and Eu) we used the spectral synthesis method due to the hyperfine structure and the contribution of different isotopes to the absorption lines. To determine the abundances of Ba and Eu we used the absorption lines of Ba II at 5853 Å and Eu II at 6645 Å, respectively. The Ba II line at 5853 Å was selected due to the small NLTE corrections obtained for this transition (Andrievsky et al. 2013; Bergemann et al. 2018). In Figure 2 we show for the target star 7 an example of the spectral syntheses and best fit abundances for the Ba II line (left panel) and the Eu II line (right panel). The atomic parameters of the iron-peak elements, as well as Na, Al and Ba were obtained from Heiter et al. (2015), Sales Silva et al. (2016) and McWilliam (1998), whereas for Eu we used the atomic parameters from M. Roriz et al. (2019, in preparation). For Cr and Na we adopted the NLTE corrections from Bergemann et al. (2014) and Lind et al. (2011), respectively. For Al I transitions analyzed, the NLTE corrections are negligible (Nordlander & Lind 2017). We note that for Ni there were no NLTE studies available in the literature.

We adopted the spherical MARCS models (Gustafsson et al. 2008) and used the MOOG code (Snedden 1973) to perform 1-D LTE analysis and generate synthetic spectra as well as compute abundances from equivalent widths (EW). For determination of the atmospheric parameters,

we used the excitation, and ionization equilibrium approaches for the Fe I and Fe II absorption lines, besides the independence of the equivalent width with the abundance of Fe I. We also did test calculations with Kurucz plane-parallel models (Kurucz 1996). In general, the stellar parameter results using the different atmospheric models (MARCS and Kurucz) were very similar with a mean difference within the uncertainties of the respective parameters: $\langle \Delta T_{\text{eff(MARCS-kurucz)}} \rangle = 49$ K, $\langle \Delta \log g_{\text{MARCS-kurucz}} \rangle = 0.1$, $\Delta \xi_{\text{MARCS-kurucz}} = 0.08$ km/s and $\langle \Delta [\text{Fe}/\text{H}]_{\text{MARCS-kurucz}} \rangle = 0.04$. We selected the MARCS models to define the final atmospheric parameters of our stars knowing that this choice would not influence our results and conclusions because both models present very similar results. In Table 2 we show the atmospheric parameters adopted for the stars of our sample. In the Appendix, we show the uncertainties associated with atmospheric parameters and chemical abundances.

As previously mentioned, for the sake of comparison we added one star observed by Bergemann et al. (2018) to our sample. The atmospheric parameters obtained for this star (#14) are also in Table 2. Our results are very similar to those obtained by Bergemann et al. (2018) for T_{eff} , ξ , and $[\text{Fe}/\text{H}]$, only for $\log g$ we found a large discrepancy ($\Delta \log g = 0.72$), with our $\log g$ being smaller than that determined in Bergemann et al. (2018). As in this study, Bergemann et al. (2018) determined $\log g$ through the ionization equilibrium of Fe I and Fe II. To further test our methodology, we determined the atmospheric parameters for the Sun and the 'standard' red giant Arcturus applying the same methodology used here for the TriAnd candidate stars, and we found values very similar to those found in the literature (see Appendix), including $\log g$.

4. RESULTS

4.1. Kinematics of TriAnd stars

The sample selection criteria used in the previous section were based on spatial position and a color-magnitude cut. However, to better identify TriAnd candidates we also apply kinematic criteria. As in Sheffield et al. (2014), we used the radial velocity in the Galac-

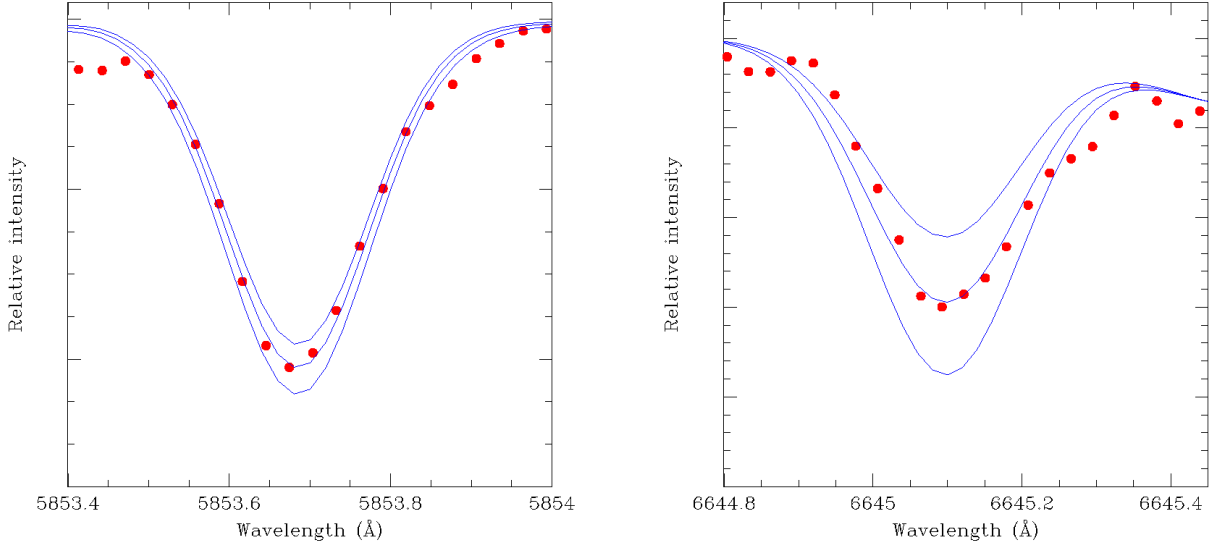


FIG. 2.— Observed (dotted red line) and synthetic spectra (solid blue lines) in the region of the Ba II and Eu II lines at 5853 Å and 6645 Å, respectively, for the star 7. The synthetic spectra in the 5853 Å region represents $[\text{Ba}/\text{Fe}] = 0.26, 0.46$ and 0.66 whereas for the 6645 Å region the synthetic spectra represents $[\text{Eu}/\text{Fe}] = 0.20, 0.40$ and 0.60 .

TABLE 2

DERIVED ATMOSPHERIC PARAMETERS, RADIAL VELOCITIES, AND METALLICITY FOR TRIAND STARS CANDIDATES. FOR $[\text{Fe I}/\text{H}]$ AND $[\text{Fe II}/\text{H}]$ WE ALSO SHOW THE STANDARD DEVIATION AND THE NUMBER OF LINES EMPLOYED.

#	T_{eff} K	$\log g$	ξ km s^{-1}	$[\text{Fe I}/\text{H}] \pm \sigma$ (#)	$[\text{Fe II}/\text{H}] \pm \sigma$ (#)	RV km s^{-1}	μ_{α}^{\ddagger} mas/yr	μ_{δ}^{\ddagger} mas/yr	Membership \dagger
1	4150	0.6	0.88	-1.71 ± 0.09 (49)	-1.70 ± 0.08 (7)	-233.6 ± 0.5	0.83 ± 0.04	-0.45 ± 0.02	Non-Member
2	3925	1.3	1.81	-0.46 ± 0.10 (39)	-0.46 ± 0.08 (5)	-245.3 ± 1.5	-0.74 ± 0.07	0.12 ± 0.05	Non-Member
3	4100	0.4	1.77	-0.82 ± 0.10 (48)	-0.81 ± 0.10 (5)	-165.6 ± 0.5	-0.15 ± 0.06	0.06 ± 0.05	Member
4	4125	0.0	1.04	-1.50 ± 0.11 (58)	-1.49 ± 0.12 (6)	-144.0 ± 0.8	1.88 ± 0.05	-0.76 ± 0.05	Non-Member
5	4075	0.7	1.99	-0.94 ± 0.10 (49)	-0.95 ± 0.16 (5)	-162.4 ± 0.5	-0.29 ± 0.08	-0.02 ± 0.09	Member
6	3900	0.5	1.82	-0.81 ± 0.13 (38)	-0.80 ± 0.07 (5)	-139.5 ± 1.4	0.20 ± 0.05	-0.20 ± 0.05	Member
7	4200	1.3	0.60	-0.78 ± 0.10 (49)	-0.78 ± 0.04 (5)	-118.6 ± 0.6	-0.44 ± 0.03	-0.72 ± 0.03	Member
8	3975	0.4	1.93	-1.42 ± 0.08 (52)	-1.40 ± 0.08 (5)	-196.9 ± 0.6	1.20 ± 0.04	-0.99 ± 0.03	Non-Member
9	4050	0.5	0.59	-1.23 ± 0.09 (44)	-1.22 ± 0.10 (5)	-139.7 ± 0.9	0.18 ± 0.06	-0.17 ± 0.06	Member
10	3925	1.4	1.96	-0.63 ± 0.10 (42)	-0.62 ± 0.16 (4)	-43.4 ± 0.6	1.75 ± 0.04	-0.49 ± 0.02	Non-Member
11	4025	0.9	1.63	-0.78 ± 0.10 (53)	-0.77 ± 0.10 (8)	-106.2 ± 0.7	-0.06 ± 0.07	-0.23 ± 0.05	Member
12	4000	0.3	0.97	-1.34 ± 0.12 (45)	-1.34 ± 0.13 (3)	-145.2 ± 1.0	0.17 ± 0.05	-0.26 ± 0.05	Member
13	4100	0.6	1.98	-1.03 ± 0.08 (46)	-1.03 ± 0.15 (7)	-182.1 ± 0.5	1.45 ± 0.07	-1.22 ± 0.06	Non-Member
14	3925	0.3	1.62	-0.91 ± 0.13 (54)	-0.89 ± 0.12 (6)	-85.1 ± 0.5	1.29 ± 0.05	-0.97 ± 0.04	Non-Member

\dagger See Subsection 4.1.

\ddagger Proper motion obtained from Gaia DR2 catalog (See Subsection 4.1).

to-centric Standard of Rest as a function of Galactic longitude as sample criterion (see Figure 3). We used the samples from Rocha-Pinto et al. (2004) and Sheffield et al. (2014) to obtain the 2σ prediction interval where a star from TriAnd overdensity should lie. According to this criterion the stars #1, #2, #10, and #13 are not members of TriAnd.

We cross-matched the sample from this work, Sheffield et al. (2014), Bergemann et al. (2018), Hayes et al. (2018), and Chou et al. (2011) with the Gaia DR2 catalog (Gaia Collaboration et al. 2016, 2018) to obtain the proper motion of TriAnd candidate stars. Figure 4 shows the proper motion of TriAnd candidates stars. We used a 1.5σ ellipsoid around the centroid of the proper motion distribution of TriAnd candidates to estimate the TriAnd characteristic proper motion. The stars #1, #2, #4, #8, #10, and #13 are outside of the ellipsoid and were classified as non-member according to their proper motion.

We call attention to the fact that the stars located in the region of the green circles #1, #4, #8, #10, #13 in Figure 4 have a randomly spatial distribution in the TriAnd region (below we discuss the orbit of these stars) while the proper motion of the other stars are varying with the longitude.

We used the Astropy library to obtain the expected proper motion for two stellar population with circular orbits situated at heliocentric distances between 18–23 kpc with $Z = -5$ and -7 kpc. These objects are distributed between $90^\circ < l < 160^\circ$ and $-15^\circ > b \approx -30^\circ$. Figure 4 shows that the expected proper motion of objects located at the position of TriAnd is compatible with the proper motion of TriAnd candidates.

As a further test to our selection criteria, we have also classified the stars according to their orbital parameters. In order to do this, we have used the stellar positions, GAIA DR2 proper motions, our measured radial veloci-

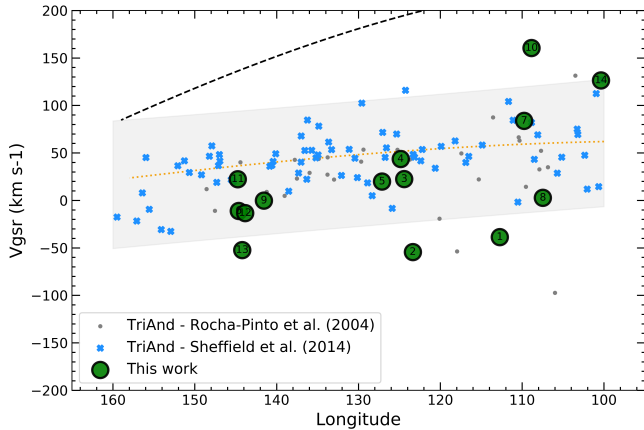


FIG. 3.— Radial velocity in the Galactocentric Standard of Rest as a function of Galactic longitude for the TriAnd candidates. The symbols in green, blue, and grey show respectively the TriAnd candidates from this work, Sheffield et al. (2014), and Rocha-Pinto et al. (2004). The dashed black line and the orange dotted curve correspond to the circular velocity[‡] for local stars and stars at $R_{GC} = 30$ kpc, respectively. The grey shaded solid region show 2σ prediction interval where the TriAnd sample would be confined. The numbers inside the green circles follow in order top-to-bottom the stars in Table 2. The stars 1, 2, 10, 13 are outside the grey area, region that indicates where the TriAnd population lie.

[‡] The rotation speed adopted is $\Theta_0 = 236 \text{ km s}^{-1}$ (Bovy, Hogg & Rix 2009) and the peculiar motion of the Sun relative to the LSR as given in Schönrich, Binney & Dehnen (2010).

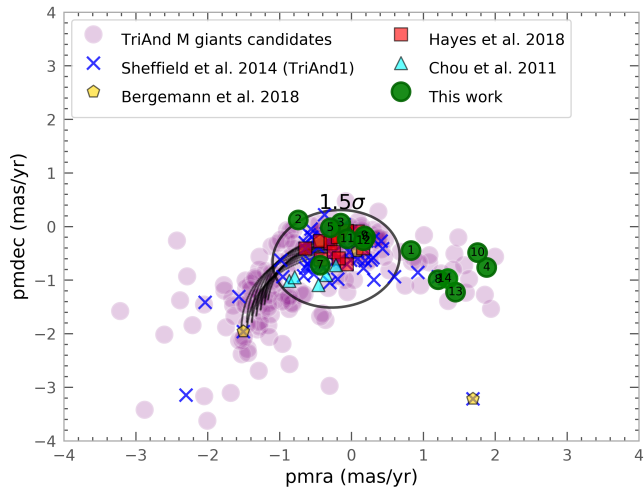


FIG. 4.— GAIA proper motion of TriAnd candidates stars. The blue crosses, green circles, yellow pentagon, red squares, and the cyan triangles, are respectively the TriAnd samples of Sheffield et al. (2014), this work, Bergemann et al. (2018), Hayes et al. (2018), and Chou et al. (2011). The purple circles are TriAnd M giants candidates without spectroscopic observation selected in the color-magnitude boxes from Sheffield et al. (2014) as describe in Section 2. The numbers inside the green circles follow in order top-to-bottom the stars in Table 2. The black dots indicate the expected proper motion for two stellar populations with heliocentric distances between 18–23 kpc with $Z = -5$ and -7 kpc. The 1.5σ ellipsoid indicates the characteristic proper motion of those samples. The stars 1, 2, 4, 8, 10, 13 are outside the ellipsoid which indicates the characteristic proper motion of TriAnd candidates

ties and our estimated distances, to integrate the stellar orbits applying the `Galpy` integrator (Bovy 2015). Distances were roughly estimated by photometric parallax. The orbits of all 14 stars in our sample can be seen in Figure 11 in Appendix C. We have also integrated the

orbits of the Bergemann et al. (2018) and Hayes et al. (2018) samples using the radial velocities and distances provided in both studies.

We characterize the orbits by defining the *eccentricity* and *orbital diskness* from the estimated perigalactic and apogalactic radius (R_{peri} , R_{apo}) and maximum distance from the galactic plane (z_{max}):

$$\text{eccentricity} = \frac{R_{\text{apo}} - R_{\text{peri}}}{R_{\text{apo}} + R_{\text{peri}}} \quad (1)$$

$$\text{orbital diskness} = \frac{R_{\text{apo}} - z_{\text{max}}}{R_{\text{apo}} + z_{\text{max}}} \quad (2)$$

By definition, the eccentricity ranges from 0 to 1 and measures how circular the projected orbit is in the galactic plane: 0 corresponds to a perfectly circular orbit, while 1 corresponds to a straight line. Similarly, the “orbital diskness” ranges from -1 to 1 and measures how confined is the stellar orbit to the galactic disk: where 1 corresponds to an orbit perfectly confined to the plane of the disk, 0 to an orbit where the vertical motion has a range equivalent to the range of the motion in the disk, and -1 when the vertical motion is much greater than the motion in the disk (a case which is very unlikely to happen to stellar orbits). These definitions allow us to characterize the stellar orbits and classify groups who display similar parameters.

The characterized orbital parameters for the 14 stars in our sample are given in Table 3. In Figure 5, we show the eccentricity and orbital diskness of our sample stars (big green squares and big black circles). The obtained orbital parameters for the stars from the samples in Chou et al. (2011), Hayes et al. (2018), and Bergemann et al. (2018) are included as well (cyan exes, red crosses, and yellow ypsilon-like symbols, respectively). To represent the location typically occupied by nearby disk stars in this diagram, we also include the Geneva-Copenhagen Survey stars (small gray circles; Casagrande et al. 2011). We see that, except for a few outliers, the stars from the Hayes et al. (2018) and Bergemann et al. (2018) occupy a very concentrated region of this diagram. We calculate the centroid of the distribution of these stars, excluding the three indicated outliers, and select all stars within a 0.2 radius around this centroid (green filled circle). Using this selection criteria, we classify as members the stars #3, #5, #6, #7, #9, #11 and #12; star #4 is not considered a member because it has a retrograde orbit and, therefore, is not kinematically similar to the other stars in the group. The stars selected by this criteria are exactly the same members selected using only the proper motions, but this has the advantage of taking into account the full 6D information regarding the stellar position and motion.

The diagram in Figure 5 seems to be particularly robust in regard to the stellar distance, which is particularly difficult to estimate for stars that are located so far away from the Sun. The stars from Bergemann et al. (2018) and Hayes et al. (2018) occupy the same location of the diagram even though the average of their reported stellar distances are very different among both samples: 13.0 and 20.0 kpc, respectively. Two stars are present in both samples: 2M00523040+3933030 and 2M01540851+3820287. They are indicated in Figure 5 by

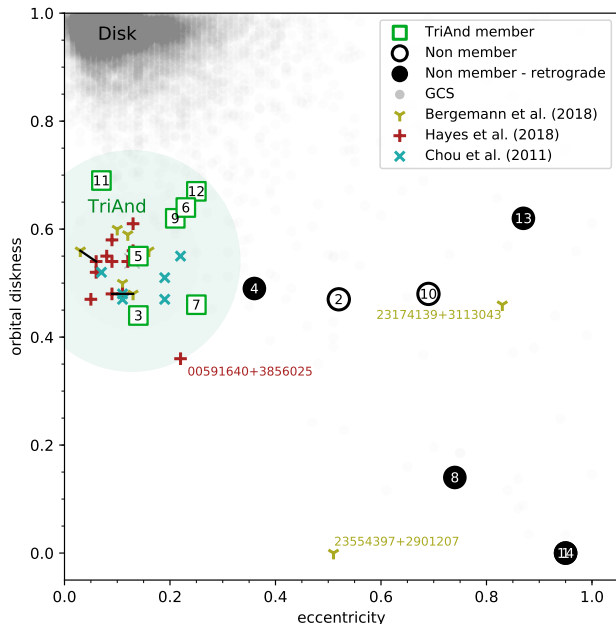


FIG. 5.— Orbital characterization through eccentricity and orbital diskness (defined in Equations 1 and 2) for the stars in our sample: the big green squares represent the stars classified as TriAnd members, while the big black circles represent the stars classified as non-members (filled black circles indicate that the star has a retrograde orbit). The stars in our sample are labeled according to the definition in Table 1. The cyan exes correspond to the Chou et al. (2011) sample, the red crosses correspond to the Hayes et al. (2018) sample and the yellow ypsilon-like symbols to the Bergemann et al. (2018) sample of classified TriAnd stars. Excluding the labelled outliers, the stars from these two samples were used to find the centroid of TriAnd in this diagram. The green filled circle represents a radius of 0.2 in eccentricity and orbital diskness around the estimated centroid and were used to select the stars. For comparison, nearby disk stars from the Geneva-Copenhagen survey are shown in grey.

the black lines connecting the red crosses and the yellow ypsilon-like symbols, and show that these orbital parameters do not change significantly for a change of a few kpc (3.0 and 3.5, kpc respectively). This result justifies our use of roughly estimated photometric parallaxes as a proxy of stellar distances, and allows us to consider the classification as very robust even though uncertainties in individual stellar distances are high.

The stars #1, #2, #10, #13 and #14 are not compatible with TriAnd population according to three different criteria. Stars #4 and #8 are not compatible in proper motion and orbital parameters. Since these stars are not members in one or more criteria we considered them as non-members of the TriAnd overdensity. We also applied the three criteria at the Bergemann et al. (2018) and Hayes et al. (2018) samples. For the Chou et al. (2011) sample we applied only the proper motion criterion as the radial velocities of the stars in their sample were not estimated. Three stars from the Bergemann et al. (2018) sample — 2M23484978+4549245, 2M23174139+3113043 (star #14), and 2M23554397+2901207 — are not inside the ellipsoid of proper motion and two of them (2M23174139+3113043 and 2M23554397+2901207) do not have the orbital characteristic similar to the other TriAnd candidates (see Figure 5). Since the star 2M23484978+4549245 from Bergemann et al. (2018) could follow the proper motion of stars at that region

(see Figure 4) and it is inside of the selection region in Figure 5, we decided not to remove this star from the sample Bergemann et al. (2018).

4.2. Chemical abundances

4.2.1. Metallicities and Iron-peak Elements

Our investigation about the chemical nature of the TriAnd overdensity starts with the analysis of the metallicities and the abundances of the iron-peak elements Cr and Ni in the target stars. SNe type Ia is the main source of enrichment of the iron peak elements (Ni and Cr, as well as Fe) in the interstellar medium (Iwamoto et al. 1999).

The TriAnd kinematically confirmed stars span the metallicity range between $-1.34 \pm 0.12 \leq [\text{Fe}/\text{H}] \leq -0.78 \pm 0.1$ dex (see Table 2), distributed in two metallicity groups, one more metal-rich group (five TriAnd stars) with $-0.94 \pm 0.1 \leq [\text{Fe}/\text{H}] \leq -0.78 \pm 0.1$ and one metal-poor group (two TriAnd stars) with $-1.34 \pm 0.12 \leq [\text{Fe}/\text{H}] \leq -1.23 \pm 0.09$ (see Figure 6); the possible distribution in two metallicity groups, however, is not considered to be significant given the small number of stars in our sample. In Figure 7 we show the metallicity distribution of the members compared to the distributions obtained in other studies for TriAnd. The metallicity distribution for the TriAnd stars of our sample (shown in green) generally agrees with the metallicity distribution of Hayes et al. (2018) (shown in red), although our distribution has a metal-poor metallicity tail. The metallicity distribution of Bergemann et al. (2018)’s sample is on average more metal-rich, in rough agreement with the average from Chou et al. (2011), although Bergemann et al. (2018) results show less scatter. It is expected that some of the differences in the metallicity results shown in Figure 6 are due, in part, to the different methodologies adopted in the different studies: different line lists, different model atmospheres, LTE versus non-LTE, optical versus infrared. For example, Bergemann et al. (2018) determined a metallicity of 0.24 dex larger than that obtained in APOGEE DR14 (Hayes et al. 2018) for the star 2M00523040+3933030, while for another star both sets of results agree. For the star #14 we derived a very similar metallicity compared to that obtained by Bergemann et al. (2018). In Figure 7 we present the metallicity distribution for all TriAnd stars analyzed with high resolution spectroscopy (our study, Chou et al. 2011, Hayes et al. 2018, Bergemann et al. 2018) and confirmed as TriAnd members through the criteria shown in subsection 4.1. The metallicity distribution for all TriAnd stars is characterized by a peak between -0.6 and -1 dex.

Interestingly, two TriAnd stars in our sample have slightly lower metallicities (star #12 with $[\text{Fe}/\text{H}] -1.34 \pm 0.12$ and star #9 with $[\text{Fe}/\text{H}] -1.23 \pm 0.09$) than those found in previous high-resolution spectroscopic studies in the literature. The metallicities of the TriAnd stars obtained in this study are, in fact, very similar to the results for TriAnd from Deason et al. (2014) obtained using low-resolution spectra from Sloan Extension for Galactic Understanding and Exploration (SEGUE). Deason et al. (2014) found a metallicity range for the TriAnd stars from -0.5 to -1.3 dex. We note that Hayes et al. (2018) also has one more metal-poor star in the APOGEE TriAnd sample ($[\text{Fe}/\text{H}] = -1.1$).

TABLE 3

THE INPUT ASTROMETRIC DATA, DISTANCES AND RADIAL VELOCITIES USED TO INTEGRATE THE STELLAR ORBITS USING THE PYTHON LIBRARY `GALPY` (BOVY 2015) AND THE OBTAINED ORBITAL PARAMETERS.

TriAnd stars																
#	ID	RA			DEC			dist kpc	pmra mas/yr	pmde mas/yr	rv km/s	R_{apo} kpc	R_{peri} kpc	z_{max} kpc	ecc	disk- ness
		hh	mm	ss.ss	dd	mm	ss.ss									
3	00594094+4614332	00	59	40.95	46	14	33.23	23.921	-0.151	0.064	-165.6	30.12	22.63	11.64	0.14	0.44
5	01151944+4713512	01	15	19.45	47	13	51.23	20.370	-0.294	-0.021	-162.4	28.39	21.30	8.16	0.14	0.55
6	02485891+4312154	02	48	58.91	43	12	15.44	16.255	0.195	-0.199	-139.5	26.23	16.28	5.85	0.23	0.64
7	23535441+3449575	23	53	54.41	34	49	57.51	10.450	-0.435	-0.721	-118.6	14.99	9.06	5.49	0.25	0.46
9	02350813+4455263	02	35	08.14	44	55	26.30	27.802	0.180	-0.174	-139.7	35.96	23.61	8.40	0.21	0.62
11	02510349+4342045	02	51	03.50	43	42	04.54	20.508	-0.061	-0.230	-106.2	29.68	25.63	5.42	0.07	0.69
12	02475442+4429269	02	47	54.42	44	29	27.00	27.608	0.166	-0.264	-145.2	37.19	22.46	7.34	0.25	0.67
Non-TriAnd stars																
1	00075751+3359414	00	07	57.51	33	59	41.42	26.306	0.827	-0.449	-233.6	31.23	0.78	30.95	0.95	0.00
2	00534976+4626089	00	53	49.77	46	26	09.00	9.977	-0.741	0.124	-245.3	22.43	7.03	7.99	0.52	0.47
4	01020943+4643251	01	02	09.43	46	43	25.13	38.988	1.881	-0.764	-144.0	83.89	39.9	28.57	0.36	0.49
8	23481637+3129372	23	48	16.38	31	29	37.21	27.074	1.205	-0.992	-196.9	30.23	4.51	22.82	0.74	0.14
10	23495808+3445569	23	49	58.08	34	45	56.92	10.667	1.753	-0.488	-43.4	19.40	3.56	6.79	0.69	0.48
13	02463235+4314481	02	46	32.36	43	14	48.15	25.194	1.445	-1.224	-182.1	33.50	2.34	7.94	0.87	0.62
14	23174139+3113043	23	17	41.39	31	13	04.33	22.191	1.294	-0.972	-85.1	30.15	0.79	30.09	0.95	0.00

TABLE 4

ABUNDANCE RATIOS([X/Fe]) FOR THE OBSERVED STARS.

TriAnd stars								
#	ID	[Na/Fe]	[Al/Fe]	[Cr/Fe]	[Ni/Fe]	[Ba/Fe]	[Eu/Fe]	[Eu/Ba]
3	00594094+4614332	0.34±0.09	0.36±0.05	—	-0.02±0.12	0.11	0.09	-0.02
5	01151944+4713512	0.36±0.12	0.38±0.05	—	0.16±0.12	0.21	0.26	0.05
6	02485891+4312154	0.16±0.14	0.39±0.07	—	0.06±0.11	0.37	0.28	-0.09
7	23535441+3449575	-0.23±0.09	0.10±0.14	-0.01	-0.03±0.09	0.46	0.40	-0.06
9	02350813+4455263	0.17±0.13	0.51±0.08	0.08	0.09±0.13	0.22	0.15	-0.07
11	02510349+4342045	0.15±0.03	0.24±0.13	-0.21	0.14±0.12	0.58	0.30	-0.28
12	02475442+4429269	0.26±0.13	0.53±0.09	-0.07	0.25±0.13	-0.11	0.26	0.37
Non-TriAnd stars								
1	00075751+3359414	-0.14±0.04	0.26±0.13	-0.13	-0.05±0.13	0.21	0.71	0.50
2	00534976+4626089	-0.09±0.03	0.12±0.13	—	0.01±0.13	0.14	0.28	0.14
4	01020943+4643251	-0.03±0.08	0.15±0.11	-0.52	0.06±0.11	0.05	0.57	0.52
8	23481637+3129372	-0.13±0.09	—	-0.23	0.02±0.12	0.17	0.84	0.67
10	23495808+3445569	-0.50±0.09	-0.31±0.12	—	-0.03±0.12	0.40	0.70	0.30
13	02463235+4314481	0.08±0.13	0.25±0.03	-0.16	-0.01±0.14	0.22	0.53	0.31
14	23174139+3113043	-0.31	0.04	-0.14	-0.17±0.14	0.42	0.70	0.28

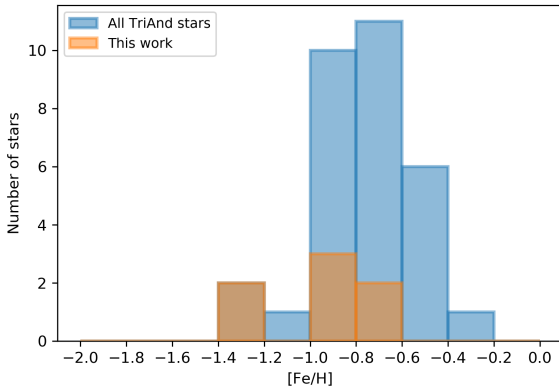


FIG. 6.— Metallicity histogram for all TriAnd stars analyzed by high-resolution spectroscopy. The metallicity distribution for our TriAnd star sample is in orange.

The TriAnd stars in our sample exhibit $[\text{Ni}/\text{Fe}]$ in the range between $-0.03 \pm 0.09 \leq [\text{Ni}/\text{Fe}] \leq +0.25 \pm 0.13$ and $[\text{Cr}/\text{Fe}]$ between -0.21 to $+0.08$ dex (Table 4); this is the first study to obtain chromium abundances in TriAnd stars. In Figure 8 the results for $[\text{Cr}/\text{Fe}]$ and $[\text{Ni}/\text{Fe}]$ are shown as a function of $[\text{Fe}/\text{H}]$ for our sample (filled red circles). We also show in this figure our results for non-TriAnd stars (as open red symbols), as well as literature results for the TriAnd stars (Chou et al. 2011, Bergemann et al. 2018, Hayes et al. 2018), local disk stars (Bensby et al. 2014), thick disk stars (Reddy et al. 2006), open clusters from the outer disk (Yong et al. 2012), cepheids from the outer disk (Luck et al. 2011, Lemasle et al. 2013 and Genovali et al. 2015), halo stars (Ishigaki et al. 2012), and stars from dwarf galaxies (Sculptor: Shetrone et al. 2003, Geisler et al. 2005; Carina: Shetrone et al. 2003, Koch et al. 2008; Fornax: Shetrone et al. 2003, Letarte et al. 2010; Sagittarius: Monaco et al. 2005, Sbordone et al. 2007). The majority of our TriAnd sample presents $[\text{Cr}/\text{Fe}]$ and $[\text{Ni}/\text{Fe}]$ ratios similar to the chemical pat-

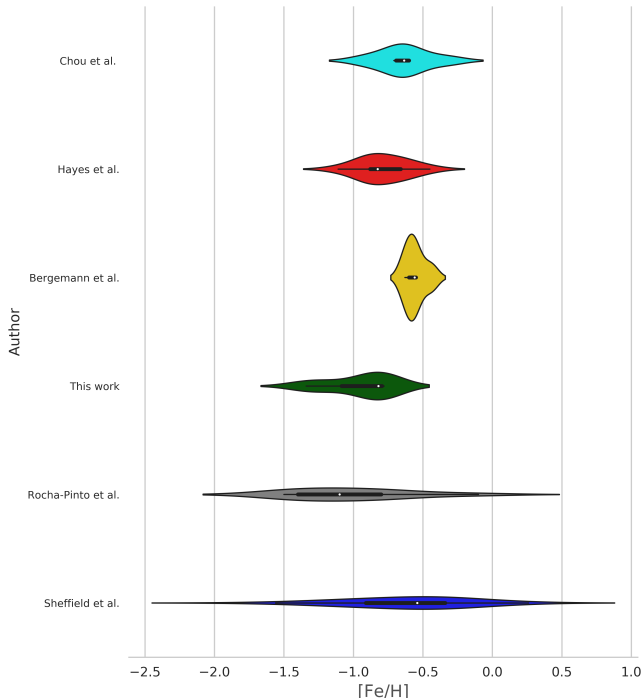


FIG. 7.— Metallicity distribution for the TriAnd stars. In cyan: Chou et al. (2011); in red: Hayes et al. (2018); in yellow: Bergemann et al. (2018); in green: this work; in grey: Rocha-Pinto et al. (2004), and in blue: Sheffield et al. (2014). In violin plots, the white dot is the median, the thick bar is the interquartile range, and the thin bar represents the 95% confidence interval. The distribution around these lines represents the distribution shape of the sample where the wider regions represent a higher probability that a star will have that metallicity.

tern of the local disk. This is case in particular for Cr. However, for Ni, the lower metallicity TriAnd stars in our sample tend to show a slight overabundance of Ni, which is not seen in the results for the local disk stars. The APOGEE results (orange triangles) do not probe such low metallicities.

Simulations indicate that Ni and Fe yields in SNe type Ia are strongly dependent on the white dwarf mass (Leung & Nomoto 2018). Thus, the slight overabundance of the $[\text{Ni}/\text{Fe}]$ ratio in the TriAnd stars of lower metallicity in relation to the local disk may be due to the mass difference of the white dwarfs that produced Ni and Fe in the TriAnd region and the local disk. In Figure 8 we see that the Sagittarius stars (blue circles) present a sub-solar $[\text{Ni}/\text{Fe}]$ ratio at $[\text{Fe}/\text{H}] = -0.8$, a chemical pattern not observed for the TriAnd stars.

4.2.2. Na and Al

Na and Al are mainly formed during the evolution of massive stars (Woosley & Weaver 1995). Na abundances in the surface of red giants is also affected by mixing processes occurring in the stellar interior (Charbonnel & Lagarde 2010).

The $[\text{Na}/\text{Fe}]$ ratio obtained for the TriAnd stars studied here spans the range from -0.23 ± 0.09 to $+0.36 \pm 0.12$ dex, with all stars, except one, exhibiting $[\text{Na}/\text{Fe}]$ ratios greater than zero (Figure 8). Most of the TriAnd stars in our sample (filled red circles) show Na overabundances when compared to the local disk stars in the same metallicity range (Figure 8), with some overlap

with the thick disk results from Reddy et al. (2006). An overabundance in $[\text{Na}/\text{Fe}]$ is also observed for the open clusters and cepheids in the outer disk (shown as yellow circles in Figure 8), although these have higher metallicities than our TriAnd sample; in addition, we note that the outer disk clusters and cepheids lie at much closer distances than the TriAnd overdensity, not probing the same region of the Galactic disk. The results from Bergemann et al. (2018) sample present a typical $[\text{Na}/\text{Fe}]$ ratio of local disk stars, such results are not necessarily inconsistent with ours, as their sample probes a higher metallicity regime for TriAnd. In addition, the non-TriAnd stars in our sample have lower $[\text{Na}/\text{Fe}]$ with a larger scatter with a behavior that is clearly distinct of the TriAnd stars.

One of our TriAnd star (star #7), however, has a much lower $[\text{Na}/\text{Fe}]$ ratio ($[\text{Na}/\text{Fe}] = -0.23 \pm 0.09$), its chemistry would indicate that it could possibly be from a different population, the $[\text{Na}/\text{Fe}]$ ratio for this star lies at the upper envelope of the dwarf spheroidal results for $[\text{Na}/\text{Fe}]$ (presented as blue symbols in Figure 8), which are much lower than the local disk. We note that such low values for $[\text{Na}/\text{Fe}]$ are also found for two additional target stars (star #10 and #14) that have not been kinematically confirmed here as part of the TriAnd overdensity. Bergemann et al. (2018) classified star #14 (for which we find $[\text{Na}/\text{Fe}] = -0.31$ and Bergemann et al. (2018) find $[\text{Na}/\text{Fe}] = -0.30$) as being from the TriAnd overdensity. However, as discussed previously, this star has a proper motion that is different from that of the other TriAnd stars, suggesting that it does not belong to TriAnd. The non-TriAnd star #10, having the lowest $[\text{Na}/\text{Fe}]$ ratio in our sample ($= -0.5 \pm 0.09$ dex; shown as the red star symbol in Figure 8), exhibits a chemical pattern in many elements similar to that of dwarf galaxy stars, showing that the field in the direction of TriAnd overdensity is composed of a stellar population mixture.

Adopting the kinematical definition for TriAnd stars in this study, the $[\text{Na}/\text{Fe}]$ results obtained would indicate that the TriAnd overdensity presents a large scatter in $[\text{Na}/\text{Fe}]$ and multiple chemical patterns, with high $[\text{Na}/\text{Fe}]$ for most stars, but with one TriAnd star having much lower $[\text{Na}/\text{Fe}]$, which is consistent with the chemical pattern of dwarf spheroidal galaxies. Despite this low $[\text{Na}/\text{Fe}]$ result, our results taken in conjunction with those from Bergemann et al. (2018), may indicate that the $[\text{Na}/\text{Fe}]$ ratio in the TriAnd population may increase slightly with the decrease in metallicity (Figure 8). (See also discussion in Smiljanic et al. (2016) that the chemical evolution of Na in the Galaxy is not well understood).

This is the first study to present aluminum abundances for TriAnd members. We find that the TriAnd stars have overabundance of Al with respect to Fe, with $[\text{Al}/\text{Fe}]$ ranging from $+0.10 \pm 0.14$ to $+0.53 \pm 0.09$ dex (Table 4). The $[\text{Al}/\text{Fe}]$ pattern in the TriAnd stars mostly overlaps with that of the thick disk stars from Reddy et al. (2006; shown as open purple symbols in Figure 8). However, the lowest metallicity stars in our sample show significantly higher values of $[\text{Al}/\text{Fe}]$ than the decreasing $[\text{Al}/\text{Fe}]$ results for $[\text{Fe}/\text{H}] < -1$ dex obtained in Bensby et al. 2014 and Ishigaki et al. 2012; the behavior of TriAnd at low metallicity seems to increase for the lowest metallicity stars probed, while it is important to note that the non-TriAnd stars in our sample show an overall a distinct

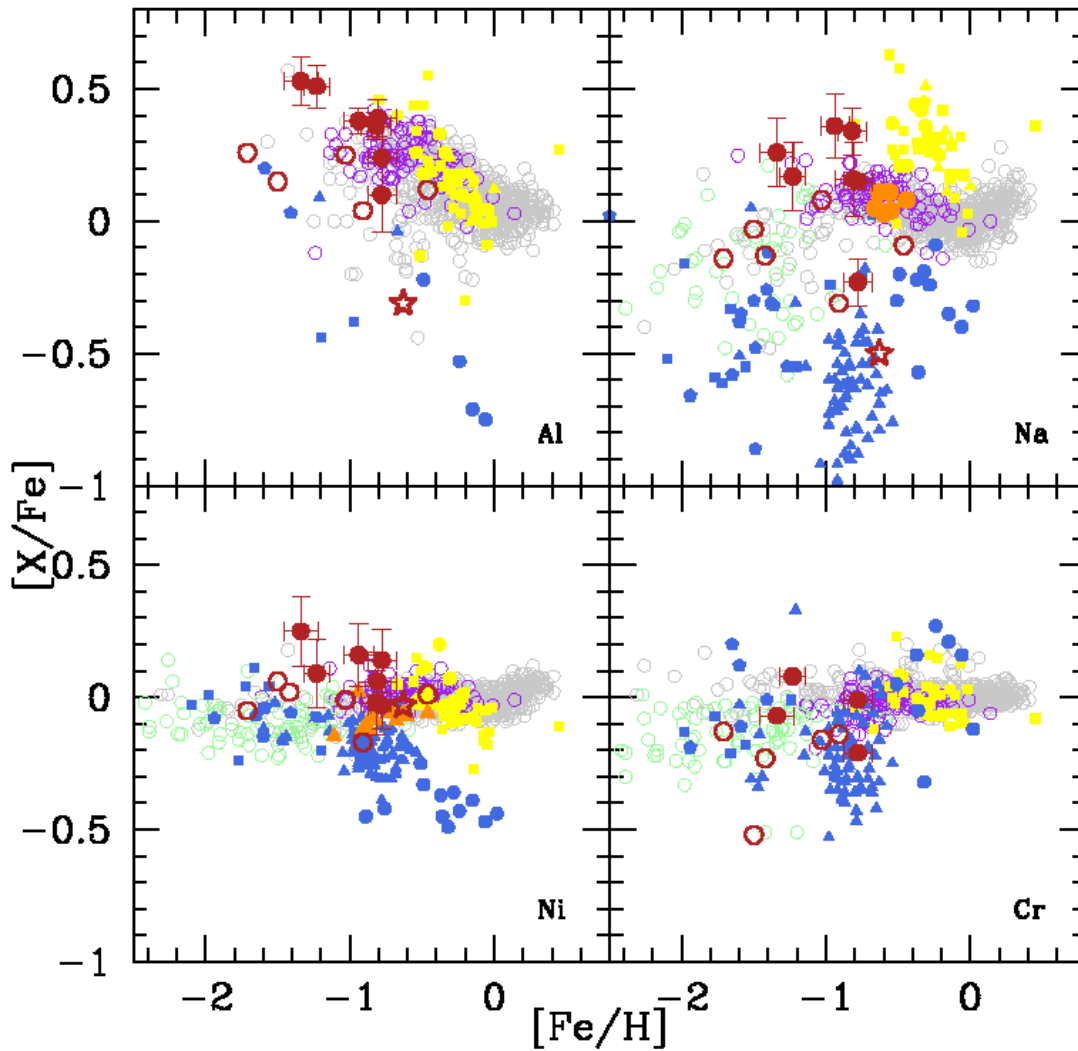


FIG. 8.— Abundance ratios $[X/Fe]$ vs. $[Fe/H]$. Red circles: our TriAnd stars sample; Open red symbols: our non-TriAnd sample; Orange triangles: TriAnd stars from Hayes et al. (2018); Orange circles: TriAnd stars from Bergemann et al. (2018); Gray circles: local disk stars from Bensby et al. (2014); Purple circles: thick disk stars from Reddy et al. (2006); Yellow circles: open clusters from the outer disk from Yong et al. (2012); Yellow squares: Cepheids from outer disk from Luck et al. (2011); Yellow hexagons: Cepheids from outer disk from Lemasle et al. (2013); Yellow triangles: Cepheids from outer disk from Genovali et al. (2015); Green circles: halo stars from Ishigaki et al. (2012); Blue squares: stars from Sculptor dwarf Galaxy from Geisler et al. (2005) and Shetrone et al. (2003); Blue hexagons: stars from Carina dwarf galaxy from Koch et al. (2008), and Shetrone et al. (2003); Blue triangles: stars from Fornax dwarf galaxy from Shetrone et al. (2003) and Letarte et al. (2010); Blue circles: stars from Sagittarius dwarf galaxy from Sbordone et al. (2007).

behavior at low metallicity. Very few results are shown in figure 8 for dwarf spheroidals; similarly to Na, it is clear that the non-TriAnd star #10 shows a low $[Al/Fe]$ value, which is consistent with dwarf spheroidals.

4.2.3. Neutron-capture Elements

The s-process elements are mainly produced during the Asymptotic Giant Branch phase (Busso et al. 1999), whereas the r-process elements are believed to be mainly produced in merging neutron stars (Thielemann et al. 2017) and possibly also in the explosive phase of type II supernovae (Thielemann et al. 2002). In general, both s- and r- processes contribute to the production of elements heavier than Fe. In this study, we derive barium and europium abundances for the target stars, to gauge the respective contributions of the s- and r- processes in

the TriAnd stars.

Table 4 presents the barium and europium results obtained for all target stars. In Figure 9 we show the derived $[Ba/Fe]$ and $[Eu/Fe]$ ratios along with the results from Bergemann et al. (2018), local disk (Bensby et al. 2014), open clusters and cepheids of the outer disk (Luck et al. 2011, Yong et al. 2012, Lemasle et al. 2013 and Genovali et al. 2015), and dwarf galaxies. The $[Ba/Fe]$ ratio for the TriAnd stars presents a large dispersion, with a range between $-0.11 - +0.58$ dex. Our results would seem to indicate that $[Ba/Fe]$ decreases with decreasing metallicity. In general, the TriAnd stars show a Ba overabundance with respect to Fe, with only one star (#12) showing a negative value of $[Ba/Fe] = -0.11$. Our $[Ba/Fe]$ results mostly overlap with those from dwarf spheroidals (in particular for metallicities higher than \sim

-1.0 dex). The results for Bergemann et al. (2018) sample of TriAnd stars (orange circles) indicate a $[\text{Ba}/\text{Fe}]$ ratio $\sim 0.18 \pm 0.06$ dex, being slightly higher than that for most of the local disk stars by Bensby et al. (2014) but still falling below the dwarf spheroidal results shown in the figure.

The $[\text{Eu}/\text{Fe}]$ ratios for all TriAnd stars in our study span the range between +0.09 to +0.40 dex, exhibiting an approximately constant trend with metallicity. The results from Bergemann et al. (2018) (orange circles) would seem to extend the roughly constant $[\text{Eu}/\text{Fe}]$ behavior towards higher metallicities. It is interesting to note that those stars in our sample that are not from TriAnd (open red circles) show a very different behavior when compared to TriAnd, including the star #10 that shows again an abundance pattern in line with those of dwarf spheroidals, in this case Fornax, having a high value of $[\text{Eu}/\text{Fe}]$. To summarize, the $[\text{Eu}/\text{Fe}]$ ratios are overall lower than results from dwarf spheroidals, showing a distinct behavior when compared to the s-process element barium that follows the pattern observed for Fornax.

The $[\text{Eu}/\text{Ba}]$ abundance ratio, a monitor of the r- and s- processes contribution in the interstellar medium that formed the TriAnd stars, is presented in Figure 10. This clearly shows how TriAnd stars segregate when compared to the disk stars. Here again the results from Bergemann et al. (2018) and from this study indicate a constant pattern for the $[\text{Eu}/\text{Ba}]$ ratios. The lowest metallicity star in our TriAnd sample (star #12) has a high $[\text{Eu}/\text{Ba}]$ ratio ($[\text{Ba}/\text{Fe}] = -0.11$ dex and $[\text{Eu}/\text{Fe}] = 0.26$ dex). Taken a face value this could indicate a higher value for $[\text{Eu}/\text{Ba}]$ for the lowest metallicities in TriAnd, but it should be kept in mind this is found for only one star in our TriAnd sample. The different $[\text{Eu}/\text{Ba}]$ ratios in the TriAnd stars may be evidence of a distinct abundance pattern for stars belonging to the TriAnd overdensity region.

4.2.4. Abundance comparisons

In order to check for possible systematic differences with the results presented in Bergemann et al. (2018) when compared to ours, we analyzed one star (#14) in common with that study and find excellent agreement in the metallicity with a difference: $\Delta [\text{Fe}/\text{H}] = 0.02$. The differences in the abundances derived for the other elements in common in the two studies are also small: $\Delta [\text{Na}/\text{Fe}] = 0.02$, $\Delta [\text{Ba}/\text{Fe}] = 0.11$, $\Delta [\text{Eu}/\text{Fe}] = 0.02$. This comparison, although for only one star, indicates similar abundance results in the two studies without any important systematic abundance differences.

5. DISCUSSION

The galactic nature of the TriAnd overdensity began to be unraveled through the high-resolution spectroscopic studies by Bergemann et al. 2018, and Hayes et al. 2018. The interactions of our Galaxy with neighboring galaxies could, for example, induce a warped and flared disk, or vertical density waves, and explain overdensities, such as TriAnd (e.g., Momany et al. 2006, Gómez et al. 2013, Bergemann et al. 2018). Bergemann et al. (2018) found that TriAnd stars have an abundance pattern similar to that of Galactic disk. The kinematic analysis presented here corroborates with the Galactic disk pattern of the TriAnd stars orbits.

The abundance results in this study indicate that the TriAnd population shows a complex chemical pattern exhibiting clear differences when compared to the local disk pattern (Bensby et al. 2014), such as, for example, for the $[\text{Na}/\text{Fe}]$ and $[\text{Ba}/\text{Fe}]$ ratios (see Figure 8, and 9).

In the following we summarize the detailed chemical pattern obtained for the sample of TriAnd stars studied here: (1) An extended metallicity distribution ranging between $[\text{Fe}/\text{H}] \sim -1.34 \pm 0.12$ to -0.78 ± 0.1 dex, which includes more metal-poor stars than the previous high-resolution studies from Chou et al. (2011), Bergemann et al. (2018), and Hayes et al. (2018). (2) The $[\text{Na}/\text{Fe}]$ ratios obtained for the TriAnd members are, for the most part, higher than the local disk. When combined with the $[\text{Na}/\text{Fe}]$ results from Bergemann et al. (2018) for higher metallicity TriAnd stars, there is an indication that $[\text{Na}/\text{Fe}]$ in the TriAnd population may increase with decreasing metallicity (Figure 8). The presence of a confirmed TriAnd star having a low $[\text{Na}/\text{Fe}]$ ratio, more similar to what is found for dwarf spheroidals, might perhaps indicate that TriAnd may have multiple populations, but this is a very speculative idea at this point. (3) The $[\text{Al}/\text{Fe}]$ ratios for TriAnd stars also exhibit an increase with the decrease in metallicity, similarly to what is observed for the local disk (Bensby et al. 2014). The two lowest metallicity TriAnd stars are an extension of the growth in the $[\text{Al}/\text{Fe}]$ ratio for $[\text{Fe}/\text{H}] < -1$. (4) The $[\text{Ni}/\text{Fe}]$ ratios for our sample of TriAnd stars show possible overabundances when compared to the local disk; for stars in the same metallicity range as the APOGEE sample in Hayes et al. (2018), our results are ~ 0.1 dex higher than the APOGEE $[\text{Ni}/\text{Fe}]$. The differences with the local disk pattern may not be significant. (5) In general, the barium in the TriAnd stars is overabundant and $[\text{Ba}/\text{Fe}]$ ratios decrease with decreasing metallicity, showing a pattern similar to that presented by dwarf spheroidals. (6) The $[\text{Eu}/\text{Fe}]$ ratios for the TriAnd stars are approximately constant with metallicity (Figure 10), this result is in line with the $[\text{Eu}/\text{Fe}]$ from Bergemann et al. (2018) for higher metallicities. (7) The $[\text{Eu}/\text{Ba}]$ ratio for the TriAnd stars in our sample have similar values those obtained in Bergemann et al. (2018) for higher metallicity TriAnd stars, indicating a roughly constant $[\text{Eu}/\text{Ba}]$ ratio with metallicity. This abundance pattern is not seen in local disk stars, with TriAnd stars showing, in general, low values when compared to the other galactic populations. Such results indicate the predominance of enrichment in s-process elements when compared to r-process elements in the gas that formed TriAnd. The high value for $[\text{Eu}/\text{Ba}]$ for the most metal-poor TriAnd star in our sample may indicate that $[\text{Eu}/\text{Ba}]$ raises with decreasing metallicity.

The metallicity distribution for all TriAnd star samples obtained using high-resolution spectroscopy (our study, Chou et al. 2011, Bergemann et al. 2018, and Hayes et al. 2018) indicates a large dispersion, having one star with a metallicities as low as $\sim -1.34 \pm 0.12$ dex (Figure 7). Given the large galactocentric distance to TriAnd ($R_{GC} \gtrsim 20$ kpc), it is of interest to compare its chemical pattern with that of the most distant stars known in the galactic disk, keeping in mind that overall the chemical pattern of the disk at galactocentric distances comparable to TriAnd ($R_{GC} \gtrsim 20$ kpc) is still unknown.

For the outer disk regions ($12 \lesssim R_{GC} \lesssim 20$ kpc), high-

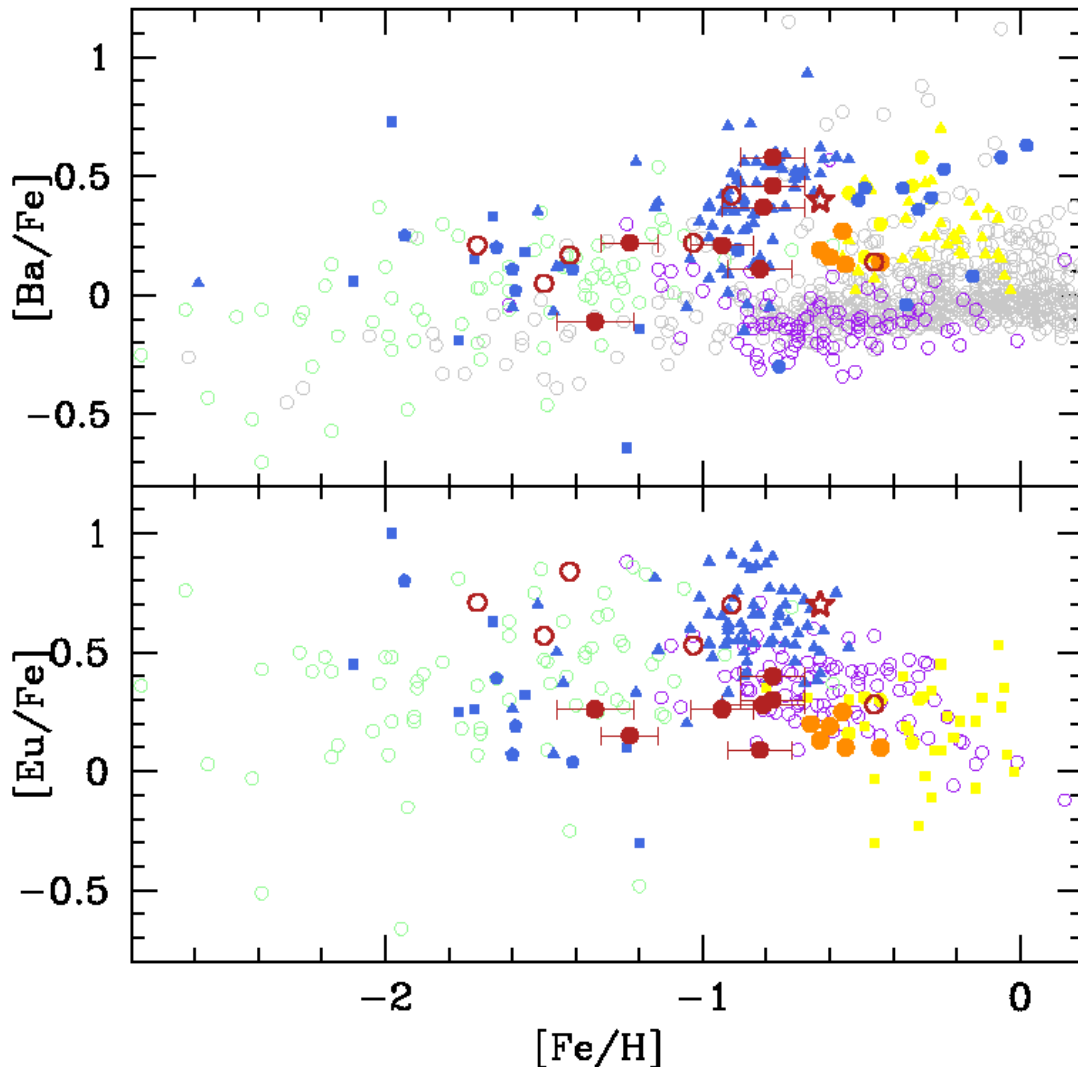


FIG. 9.— Abundance ratios $[X/Fe]$ vs. $[Fe/H]$. Symbols have the same meaning as in Figure 8. Yellow triangles in upper panel: Cepheids from outer disk from Andrievsky et al. (2014).

resolution spectroscopic studies of Cepheids, open clusters and field red giants (Andrievsky et al. 2002, Luck et al. 2003, Carraro et al. 2004, Yong et al. 2005, Carney et al. 2005, Yong et al. 2006, Bensby et al. 2011, Yong et al. 2012, Lemasle et al. 2013, Hayden et al. 2015, Cantat-Gaudin et al. 2016, Reddy et al. 2016, Carraro et al. 2017, Magrini et al. 2017) show that the metallicities of these populations cover a range roughly between $-0.8 \leq [Fe/H] \leq -0.2$ dex; this is more metal rich than the metallicity range exhibited by the TriAnd stars in our sample ($-1.34 \pm 0.12 \leq [Fe/H] \leq -0.78 \pm 0.1$) and most of APOGEE TriAnd sample discussed in Hayes et al. (2018) (Figure 7). Considering the metallicities shown in Figure 7 for the combined TriAnd samples and the discussion from Hayes et al. (2018) of the metallicities and chemical abundances for field red giants located at different galactocentric distances in the APOGEE survey, we find that the mean metallicity for the TriAnd stars is overall consistent with the extrapolated abundance gradients in the outer disk.

TriAnd stars present high $[Na/Fe]$ and $[Ba/Fe]$ ra-

tios when compared with the local disk (Figure 8, and 9). Similarly what is found for the TriAnd stars, the Cepheids and open clusters of the outer disk ($12 \text{ kpc} \lesssim R_{GC} \lesssim 20 \text{ kpc}$) also present $[Na/Fe]$ and $[Ba/Fe]$ greater than the local disk, although the Cepheids and open clusters are more metal-rich than TriAnd. In addition, concerning the patterns for the elements Al, Na, Ni, Ba and Eu, TriAnd could be considered as an extension to lower metallicities of the abundance trends $[X/Fe]$ ratios of outer disk between $12 \text{ kpc} \lesssim R_{GC} \lesssim 20 \text{ kpc}$. The $[Ba/Fe]$ ratio of the TriAnd stars also resembles the pattern presented by the Fornax dwarf galaxy, however, we observe significant differences between these populations for other elements (like Na). We detected one Non-TriAnd star with a chemical abundance that resembles dwarf galaxies in the direction of the TriAnd overdensity (see the star symbol referring to the Non-TriAnd star 10 in Figures 8, 9 and 10) indicate that such regions may suffer from pollution of dwarf galaxies as also found by Chou et al. (2011).

Modeling the chemical evolution of the outermost re-

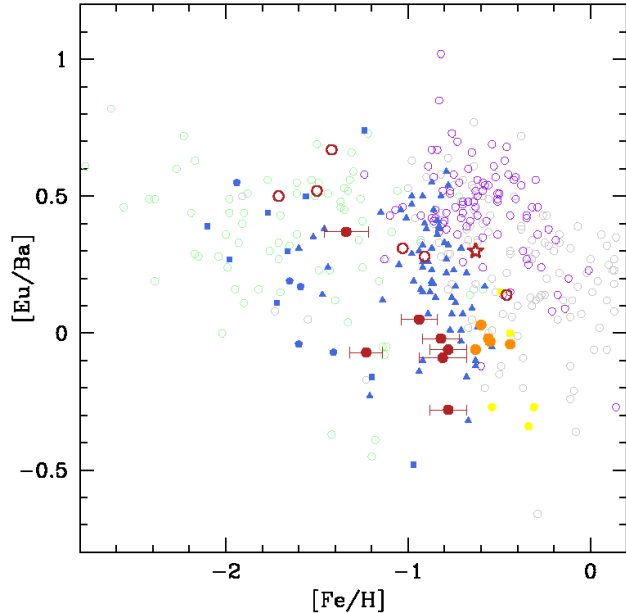


FIG. 10.— Abundance ratios $[\text{Ba}/\text{Eu}]$ vs. $[\text{Fe}/\text{H}]$. Symbols have the same meaning as in Figure 8. The open gray circles represent the local disk stars from Edvardsson et al. (1993), Nissen, & Schuster (1997), Hanson et al. (1998), Prochaska et al. (2000), Fulbright (2000), Fulbright (2002), Stephens, & Boesgaard (2002), Bensby et al. (2003), and Reddy et al. (2003), as compiled by Venn et al. (2004).

regions of the Galactic disk is challenging given, on the one hand, the variety of mechanisms that influence the evolution of the outer Galaxy, and, on the other, the few high-resolution spectroscopic observations of stars in this region to constrain the models. The high uncertainty associated with the age and distance of the stars, even currently in the era of GAIA astrometric data, is a further complication.

One of the most promising hypotheses to explain the TriAnd overdensity would be disk disruption caused by the interaction of the Galaxy with its neighbors (Bergemann et al. 2018), similar interactions were found in other spiral galaxies, such as ESO 510-G13 and NGC 1512 (López-Sánchez et al. 2015). In addition to interactions and mergers between galaxies, other mechanisms could perhaps be invoked to contribute to the chemical abundance patterns of outer disks, such as, stellar radial migration (Sellwood & Binney 2002), galactic winds (e.g., Zhang 2018), as well as possible differences in the Initial Mass Function (IMF) and star formation rate, due to regions of lower gas densities in the outer disk when compared to the innermost disk regions. The abundance patterns of the stars in the TriAnd overdensity obtained in this study, which is somewhat unique when compared to any other galactic population at its metallicity, highlight this complexity, indicating that many variables need to be considered for modeling this region. The next step in further understanding the nature TriAnd overdensity is the reliable homogeneous analysis of a much larger sample of this population; as well as other populations of the outer Milky Way disk, at $R_{GC} \sim 20$ kpc and beyond; the outer disk remains an unexplored territory that starts to be unraveled.

6. CONCLUSIONS

The Triangulum–Andromeda (TriAnd) overdensity is a distant structure of the Milky Way ($R_{GC} \sim 20 - 30$ kpc) located in the second Galactic quadrant well below the Galactic plane (Rocha-Pinto et al. 2004; Majewski et al. 2004).

We analysed high-resolution optical spectra obtained with the GRACES spectrograph on the Gemini-N telescope and derived stellar metallicities and stellar parameters from a sample of 170 Fe I and Fe II lines with atomic parameters obtained from Heiter et al. (2015). We derived the abundances of the elements Al, Na, Ni, Cr, as well as the heavy-elements Ba (s-process element) and Eu (r-process element).

We observed 13 candidate member stars in the TriAnd overdensity. Seven stars were confirmed as members of this population through a kinematic analysis and computation of stellar orbits using GAIA DR2 (Gaia Collaboration et al. 2018) proper motions along with our measured radial velocities of the stars. We also evaluated the membership of 17 additional TriAnd candidates analyzed in the previous high-resolution studies of Bergemann et al. (2018) and Hayes et al. (2018), finding that two of these stars are probably not TriAnd members given their proper motions and orbit eccentricities.

One of the results of this study is the confirmation that the TriAnd overdensity has low-metallicity stars: our TriAnd sample has metallicities ranging from $[\text{Fe}/\text{H}] = -1.34 \pm 0.12$ to -0.78 ± 0.1 dex, in contrast with the mono-metallicity of the TriAnd sample analyzed in Bergemann et al. (2018) ($\langle [\text{Fe}/\text{H}] \rangle = -0.57 \pm 0.08$). Our sample also extends to lower metallicities than the APOGEE sample (Hayes et al. 2018; their lowest metallicity star has $[\text{Fe}/\text{H}] \approx -1.1$ dex).

We find that the TriAnd overdensity is a structure composed of stars having disk-like orbits and a unique chemical pattern that does not entirely resemble the full abundance pattern observed for the stars in the local Galactic disk, nor dwarf spheroidal galaxies. TriAnd stars in our sample exhibit differences in the abundance patterns of $[\text{Na}/\text{Fe}]$, $[\text{Al}/\text{Fe}]$, (marginally $[\text{Ni}/\text{Fe}]$), $[\text{Ba}/\text{Fe}]$ and $[\text{Eu}/\text{Fe}]$, when compared to the Milky Way trend. In particular, the heavy-element abundance ratios of $[\text{Eu}/\text{Ba}]$ indicate that TriAnd is distinct, having low $[\text{Eu}/\text{Ba}]$ ratios for all stars in our study; similar low values of $[\text{Eu}/\text{Ba}]$ ratios are also found in Bergemann et al. (2018). The exception is the most metal-poor TriAnd star in our sample, for which the $[\text{Eu}/\text{Ba}]$ ratio is higher.

It should be noted that those target stars found to be non-TriAnd members based on a kinematic analysis generally exhibit a distinct chemical behavior when compared to the confirmed TriAnd members; the non-TriAnd stars have a chemical pattern that most closely resembles the chemical pattern of the local disk or halo. In addition one of the non-members stars can be chemically tagged to dwarf galaxy population as its abundances completely agree with the dwarf spheroidal pattern. The targets that ended up not being from TriAnd serve as surrogate comparison stars and play an important role in the validation of the abundance offsets. The fact that we can chemically tag the TriAnd versus the non-TriAnd stars boosts confidence that the abundance differences found for TriAnd are not due to systematic differences in the

abundance analyses. For its metallicity, TriAnd has a chemical pattern that is distinct from any known Galactic population. However, the chemical pattern of field stars in the very distant galaxy has not yet been fully probed.

The complexity of the abundance pattern for stars in the TriAnd overdensity, combined with the low number of TriAnd stars observed using high-resolution spectroscopy to date, and the paucity of studies chemically characterizing the outer disk population of Milky Way, are the main obstacles in unequivocally establishing the origin of the TriAnd population. Despite these barriers, the results in this paper find differences in the chemical patterns of TriAnd and the local Galactic disk, having a pattern that is also different from that of dwarf spheroidals.

We thank Allyson Sheffield for providing the metallicity data used in Sheffield et al. (2014) and Adrian M. Price-Whelan for the helpful comments about the Astropy library. We thank Maria Bergemann for ex-

tensive discussions. KC thanks Kathryn Johnston, and Chris Hayes for discussions. JVSS thanks FAPERJ proc. 202.756/2016. HDP, HJR-P and FA-F thank the Brazilian Agency CAPES for the financial support of this research. HDP thanks FAPESP proc. 2018/21250-9 This work has made use of data from the European Space Agency (ESA) mission *Gaia* (<https://www.cosmos.esa.int/gaia>), processed by the *Gaia* Data Processing and Analysis Consortium (DPAC, <https://www.cosmos.esa.int/web/gaia/dpac/consortium>). Funding for the DPAC has been provided by national institutions, in particular the institutions participating in the *Gaia* Multilateral Agreement.

Facilities: Gemini North: GRACES, ESO-Archive: VLT: UVES.

Softwares: **Astropy** (Astropy Collaboration et al. 2013, 2018) **IRAF** **Opera** **matplotlib** (Hunter et al. 2007), **Numpy** (Van Der Walt et al. 2011), **Scipy** (Jones et al. 2011).

APPENDIX

ABUNDANCE AND ATMOSPHERIC PARAMETERS UNCERTAINTIES

The uncertainty in the effective temperature was estimated from the uncertainty in the slope of the excitation potential versus abundance plot (which defined the excitation equilibrium) obtained by varying only the effective temperature until the slope increased by sigma. In the same way, the uncertainty in the slope of the equivalent width versus abundance plot defined the uncertainty in the microturbulence velocity. The $\log g$ uncertainty was determined by varying the $\log g$ until the abundance of Fe II (which defined the ionization equilibrium) increased by sigma. We performed these uncertainty steps for the star 11 and used it as a reference for the other stars in our sample. Thus we define 75 K, 0.2 dex and 0.1 km/s as the uncertainties of T_{eff} , $\log g$ and ξ , respectively, for the stars of our sample.

To calculate the uncertainties in the abundances we first determined the uncertainties caused independently by each atmospheric parameter varying these parameters of their respective uncertainties. After this, we obtained the final uncertainties of chemical abundances adding quadratically the uncertainties in abundance relative to each atmospheric parameter. In Table 5 we show the uncertainties regarding the star 11. For the other stars in our sample we have similar uncertainties.

TABLE 5
ABUNDANCE UNCERTAINTIES FOR STAR 11.

Element	ΔT_{eff} +75 K	$\Delta \log g$ +0.2	$\Delta \xi$ +0.1 km s ⁻¹	$(\sum \sigma^2)^{1/2}$
Fe I	-0.01	+0.05	-0.05	0.07
Fe II	-0.13	+0.12	-0.02	0.18
Na I	+0.07	+0.01	-0.03	0.08
Al I	+0.05	+0.01	-0.02	0.05
Cr I	+0.10	+0.03	-0.11	0.15
Ni I	-0.02	+0.06	-0.03	0.07
Ba II	+0.04	+0.10	-0.10	0.15
Eu II	-0.01	+0.10	-0.02	0.10

Notes. Each column gives the variation of the abundance caused by the variation in T_{eff} , $\log g$ and ξ . The last column gives the compounded rms uncertainty of the second to fourth columns.

CHEMICAL ABUNDANCES OF THE SUN AND ARCTURUS

We also analyzed the Arcturus and Sun spectra to test our methodology and list. The atmospheric parameters obtained for Arcturus are very similar with the results derived by Ramírez & Allende Prieto (2011), with difference of 84 K for T_{eff} , 0.04 for $\log g$, 0.1 km/s for ξ and 0.07 dex for [Fe/H]. For the Sun we determined $T_{\text{eff}} = 5820$ K, $\log g = 4.5$, and $\xi = 1.04$ km/s. Smiljanic et al. (2014) tested all the methodologies used in the GAIA-ESO survey with star references, such as Arcturus. The difference between our atmospheric parameters for Arcturus is lower than the difference of the parameters obtained by several GAIA-ESO methodologies, giving reliability to our methodology.

In Table 6 we show our results for the chemical abundance of all elements for Arcturus and the Sun. The chemical abundance for Na, Al, Ni, and r- and s-process elements for Arcturus in our study present similar values with the results of Ramírez & Allende Prieto (2011), with a difference smaller than 0.08 dex. Ramírez & Allende Prieto (2011) did not perform NLTE corrections in Cr abundances that are of the order of 0.2 (dex) in Arcturus (Bergemann & Nordlander 2014), which justifies the difference in the abundance of this element between our results and those of Ramírez & Allende Prieto (2011). Our abundance results for the Sun also present values similar to those in the literature (Table 6). We used our solar abundance to normalize the chemical abundances of all elements.

TABLE 6
ARCTURUS AND SOLAR ABUNDANCES.

Element	Sun			Arcturus		Notes.
	This work	Grevesse & Sauval (1998)	Asplund et al. (2009)	This work	Ramirez & Allende Prieto (2011)	
Fe	7.50	7.50	7.50	6.91	6.98	
Na	6.24	6.33	6.24	5.78	5.81	
Al	6.51	6.47	6.45	6.26	6.25	
Cr	5.86	5.67	5.64	5.24	4.99	
Ni	6.24	6.25	6.22	5.71	5.73	
Ba	2.25	2.13	2.18	1.53	1.50 ^a	
Eu	0.59	0.51	0.52	0.33	0.25 ^b	

^a Ba abundance from Smith et al. (2000). ^b Eu abundance for 6645Å line from Overbeek et al. (2016).

STELLAR ORBITS

In this appendix we present the stellar orbits integrated for the stars in our sample, and that were used to derive the results shown in Section 4.1. The orbits were integrated for 3.5 Gyr considering a Milky Way potential approximated as a combination of a power law with cut off bulge, a Miyamoto-Nagai disk, and a Navarro-Frenk-White halo. The integration was made using the orbital integrator `galpy` (Bovy 2015).

The input parameters for the integration are the stellar position, Gaia’s proper motion, our measured radial velocities through spectroscopy and our estimated distances through photometric parallax. The orbits were characterized in terms of eccentricity and orbital diskness (Equations 1 and 2) in order to select the TriAnd members 5.

In Figure 11, we show the orbits of all 13 stars in our sample, both in the XY disk plane, and in the XZ plane. The stars classified as members both by the proper motion and orbital parameters criteria are shown in green, and the black orbits corresponds to the stars classified as non-members by both methods (dashed lines further indicate that the orbit is retrograde).

EQUIVALENT WIDTH MEASUREMENTS

REFERENCES

- Astropy Collaboration, Robitaille, T. P., Tollerud, E. J., et al. 2013 *A&A*, 558, A33
- Astropy Collaboration, Price-Whelan, A. M., Sipócz, B. M., Günther, H. M., et al. 2018, *AJ*, 156, 123
- Andrievsky, S. M., Kovtyukh, V. V., Luck, R. E., et al. 2002, *A&A*, 392, 491
- Andrievsky, S. M., Lépine, J. R. D., Korotin, S. A., et al. 2013, *MNRAS*, 428, 3252
- Andrievsky, S. M., Luck, R. E., & Korotin, S. A. 2014, *MNRAS*, 437, 2106
- Arlandini, C., Käppeler, F., Wisshak, K., et al. 1999, *ApJ*, 525, 886
- Asplund, M., Grevesse, N., Sauval, A. J., & Scott, P. 2009, *ARA&A*, 47, 481
- Belfiore, F., Maiolino, R., & Bothwell, M. 2016, *MNRAS*, 455, 1218
- Belokurov V., 2013, *NewAR*, 57, 100
- Belokurov, V., Evans, N. W., Bell, E. F., et al. 2007, *ApJ*, 657, L89
- Belokurov, V.; Zucker, D. B.; Evans, N. W. et al. 2007 *ApJ*, 654, 897
- Bensby, T., Feltzing, S., & Lundström, I. 2003, *A&A*, 410, 527.
- Bensby, T., Feltzing, S., & Lundström, I. 2004, *A&A*, 421, 969
- Bensby, T., Alves-Brito, A., Oey, M. S., Yong, D., & Meléndez, J. 2011, *ApJ*, 735, L46
- Bensby, T., Feltzing, S., & Oey, M. S. 2014, *A&A*, 562, A71
- Bergemann, M., Ruchti, G. R., Serenelli, A., et al. 2014, *A&A*, 565, A89
- Bergemann, M., & Nordlander, T. 2014, arXiv:1403.3088
- Bergemann, M., Sesar, B., Cohen, J. G., et al. 2018, *Nature*, in press
- , Bernard, E. J.; Ferguson, A. M. N.; Schlafly, E. F.; et al. 2016, *MNRAS*, 463, 1759
- Bovy J., Hogg D. W., Rix H.-W., 2009, *ApJ*, 704, 1704
- Bovy J., 2015, *ApJS*, 216, 29
- Bresolin, F., Ryan-Weber, E., Kennicutt, R. C., & Goddard, Q. 2009, *ApJ*, 695, 580
- Bresolin, F. 2017, *Outskirts of Galaxies*, 434, 145
- Busso, M., Gallino, R., & Wasserburg, G. J. 1999, *ARA&A*, 37, 239
- Cantat-Gaudin, T., Donati, P., Vallenari, A., et al. 2016, *A&A*, 588, A120
- Carney, B. W., Yong, D., Teixeira de Almeida, M. L., & Seitzer, P. 2005, *AJ*, 130, 1111
- Carraro, G., Bresolin, F., Villanova, S., et al. 2004, *AJ*, 128, 1676
- Carraro, G., Sales Silva, J. V., Moni Bidin, C., & Vazquez, R. A. 2017, *AJ*, 153, 99
- Casagrande, L., Schnrich, R., Asplund, M., et al., 2011, *A&A*, 530, A138
- Charbonnel, C., & Lagarde, N. 2010, *A&A*, 522, A10
- Choi, J., Dotter, A., Conroy, C., et al. 2016, *ApJ*, 823, 102
- Chou, M.-Y., Majewski, S.R., Cunha, et al., 2011 *ApJ*, 731, 30
- Cutri, R. M., Skrutskie, M. F., van Dyk, S., et al. 2003, 2MASS All Sky Catalog of point sources.
- Deason, A. J., Belokurov, V., Hamren, K. M., et al. 2014, *MNRAS*, 444, 3975

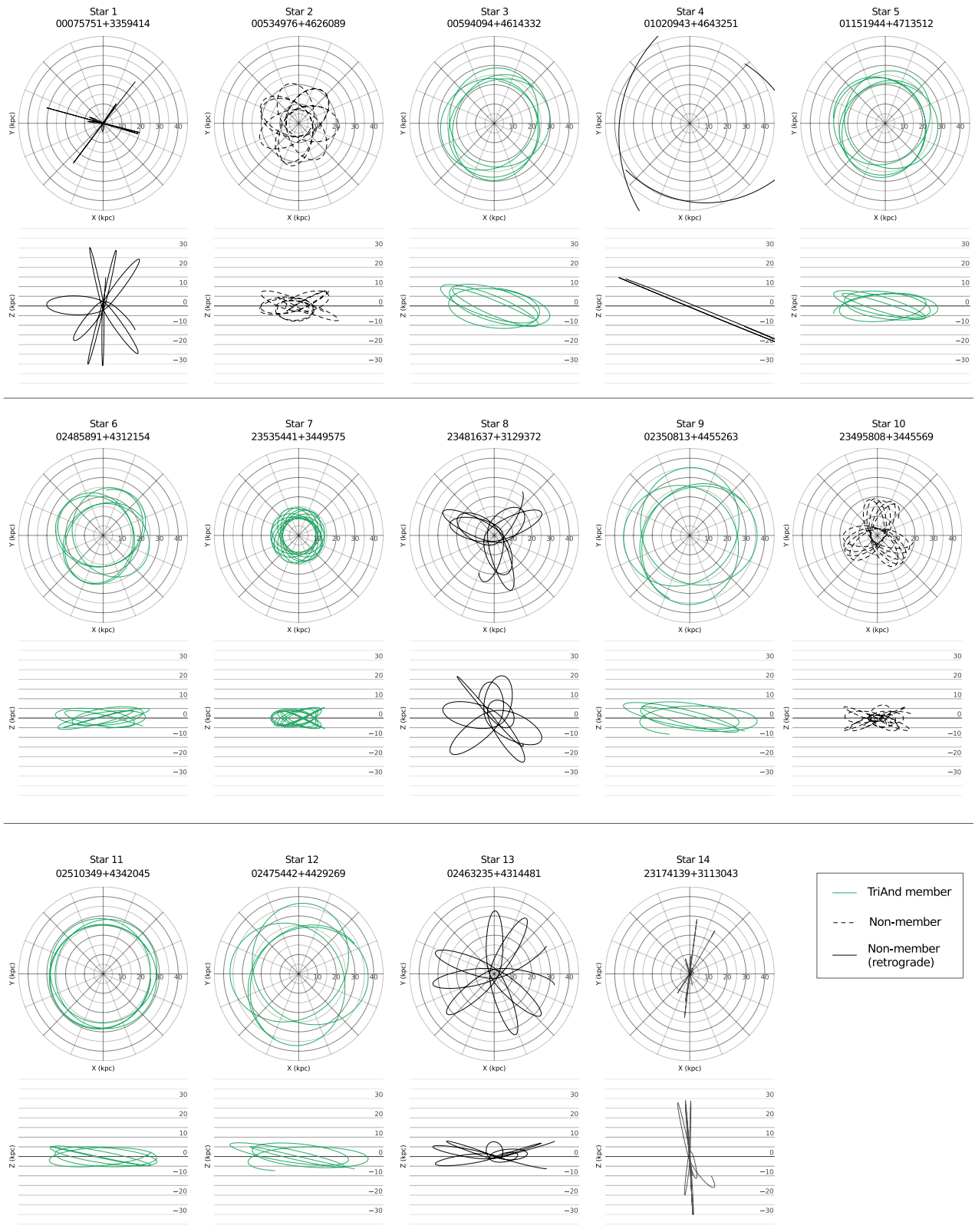


FIG. 11.— Orbits integrated for all 13 stars in our sample shown in the XY and XZ plane. The orbits of stars classified as members of TriAnd are shown in green while the non-members are shown in black. The dashed line indicate that the orbit is retrograde.

TABLE 7
OBSERVED FE I AND FE II LINES.

Element	λ (Å)	χ (eV)	$\log gf$	Equivalent Widths (mÅ)													
				Star													
				1	2	3	4	5	6	7	8	9	10	11	12	13	14
Fe I	5125.12	4.22	-0.140	—	—	—	69	—	—	81	—	75	146	—	—	—	—
	5133.69	4.18	0.360	—	—	—	—	—	—	—	—	89	—	—	—	—	—
	5159.06	4.28	-0.820	—	—	102	—	—	—	—	—	—	—	—	—	—	90
	5162.27	4.18	0.020	—	146	—	—	144	142	—	124	—	—	143	—	—	—
	5242.49	3.63	-0.967	—	—	—	—	—	—	—	105	—	—	120	—	—	115
	5250.21	0.12	-4.933	—	—	—	131	—	—	117	—	—	—	—	132	—	—
	5253.02	2.28	-3.840	—	102	97	40	—	—	63	—	84	81	—	—	—	84
	5288.52	3.69	-1.493	—	117	113	—	—	97	—	—	—	115	—	—	95	82
	5302.30	3.28	-0.738	—	—	—	—	—	—	—	146	—	—	—	—	—	—
	5315.07	4.37	-1.650	—	51	—	—	—	—	—	20	24	—	52	21	34	31
	5321.11	4.43	-1.089	—	—	77	—	74	—	—	36	—	—	61	32	—	—
	5322.04	2.28	-2.802	—	—	—	—	142	—	—	—	—	144	—	—	—	139
	5364.87	4.45	0.228	—	—	133	—	133	—	—	116	—	—	—	—	132	116
	5367.47	4.42	0.444	—	—	—	—	—	—	—	—	—	—	—	—	—	121
	5369.96	4.37	0.536	—	—	—	—	—	—	—	130	—	—	—	—	—	134
	5373.71	4.47	-0.710	—	—	91	37	84	—	—	65	—	89	89	54	83	79
	5389.48	4.42	-0.410	47	119	119	61	109	107	71	—	—	—	—	63	—	—
	5400.50	4.37	-0.160	61	—	—	—	—	—	—	—	—	—	—	—	—	—
	5410.91	4.47	0.398	—	—	139	—	135	—	—	—	—	—	—	—	138	—
	5417.03	4.42	-1.580	13	55	47	14	—	43	26	24	25	47	45	—	36	35
	5441.34	4.31	-1.630	—	51	—	13	—	—	—	—	—	—	54	20	—	—
	5445.04	4.39	-0.020	—	—	—	—	—	—	—	114	—	131	117	—	129	113
	5487.74	4.32	-0.317	—	—	—	59	—	—	83	—	—	—	—	—	—	—
	5522.45	4.21	-1.450	20	—	—	28	68	—	—	38	37	62	61	33	61	51
	5532.75	3.57	-2.050	—	—	—	34	—	—	59	—	49	96	—	—	—	85
	5554.89	4.55	-0.270	46	120	115	47	106	111	71	78	61	—	—	59	103	97
	5560.21	4.43	-1.090	19	70	—	26	81	—	—	—	33	—	61	—	67	55
	5567.39	2.61	-2.568	—	—	—	71	139	146	76	—	70	—	—	82	—	—
	5576.09	3.43	-0.900	—	—	—	—	—	—	—	—	—	—	140	—	—	141
	5584.77	3.57	-2.220	—	91	—	27	—	86	—	46	—	—	66	—	82	68
	5624.02	4.39	-1.380	—	73	—	—	—	—	45	—	—	68	—	—	—	52
	5633.95	4.99	-0.230	23	79	86	37	69	77	47	—	42	74	70	42	75	67
	5635.82	4.26	-1.790	14	57	—	—	—	52	—	25	27	54	—	—	—	—
	5638.26	4.22	-0.720	43	111	108	—	111	103	65	78	57	107	102	—	114	92
	5658.82	3.40	-0.766	93	—	—	—	—	—	—	—	99	—	—	—	—	—
	5686.53	4.55	-0.455	39	—	102	42	104	87	—	74	53	—	87	53	88	77
	5691.50	4.30	-1.450	22	69	78	16	65	56	42	—	33	69	67	35	—	49
	5705.46	4.30	-1.355	18	71	62	25	—	69	—	44	—	70	—	36	—	44
	5717.83	4.28	-0.990	30	—	—	—	—	—	—	—	—	—	83	—	78	64
	5731.76	4.26	-1.200	—	—	85	—	—	—	—	—	39	80	77	—	—	61
	5762.99	4.21	-0.360	—	—	132	66	130	137	84	112	72	—	—	85	134	—
	5806.73	4.61	-0.950	24	74	70	—	66	60	48	45	38	74	69	42	69	—
	5814.81	4.28	-1.870	—	53	47	11	49	54	26	—	—	50	40	25	—	—
	5883.82	3.96	-1.260	—	100	96	—	105	—	—	77	—	—	91	—	—	87
	5916.25	2.45	-2.994	59	133	138	73	129	135	79	114	72	136	125	79	123	113
	5934.65	3.93	-1.070	54	—	116	—	126	119	75	96	69	—	111	—	110	109
	6016.60	3.55	-1.720	49	—	—	65	—	—	—	—	—	—	—	—	—	—
	6020.17	4.61	-0.270	42	—	—	—	—	—	—	—	—	—	—	—	—	—
	6024.06	4.55	-0.120	62	124	—	57	118	—	—	—	—	—	114	—	117	103
	6027.05	4.08	-1.089	—	110	—	48	93	—	—	83	—	—	90	—	98	79
	6056.01	4.73	-0.320	—	—	—	38	—	—	—	63	—	—	—	53	89	—
	6065.48	2.61	-1.529	112	—	—	128	—	—	127	—	—	118	—	—	127	—
	6079.01	4.65	-1.020	21	—	65	21	65	53	40	32	37	53	56	39	60	48
	6082.71	2.22	-3.576	57	—	114	68	—	133	74	97	70	—	113	81	—	111
	6093.64	4.61	-1.400	—	60	48	—	36	—	31	25	24	43	41	—	—	—
	6096.66	3.98	-1.830	18	68	75	31	75	68	45	—	41	64	63	—	66	50
	6120.25	0.92	-5.970	33	101	92	47	98	105	55	63	52	100	88	66	88	94
	6136.61	2.45	-1.402	126	—	—	149	—	—	—	—	146	—	—	—	—	—

Table 6, continued.

Element	λ (Å)	χ (eV)	$\log gf$	Equivalent Widths (mÅ)													
				Star													
				1	2	3	4	5	6	7	8	9	10	11	12	13	14
Fe I	6151.62	2.18	-3.295	67	141	141	82	146	149	79	129	80	148	135	85	137	136
	6157.73	4.08	-1.160	44	—	—	53	111	—	—	—	—	—	—	—	—	—
	6165.36	4.14	-1.473	28	84	81	28	76	82	52	50	36	—	70	37	67	60
	6173.33	2.22	-2.880	78	—	—	—	—	—	94	—	86	—	140	—	—	—
	6187.99	3.94	-1.620	—	100	86	35	77	—	—	—	—	75	85	43	72	74
	6191.56	2.43	-1.416	—	—	—	135	—	—	146	—	—	—	—	—	—	—
	6200.31	2.61	-2.433	—	—	—	—	144	—	—	133	—	149	131	—	147	131
	6213.43	2.22	-2.481	—	—	—	112	—	—	108	—	103	—	—	—	—	—
	6252.56	2.40	-1.699	121	—	—	—	—	—	147	—	132	—	—	140	—	—
	6254.26	2.28	-2.439	—	—	—	—	—	—	—	—	—	—	—	123	—	—
	6311.50	2.83	-3.141	—	—	—	49	92	86	60	67	48	—	76	51	93	81
	6322.69	2.59	-2.430	—	—	—	99	—	146	—	140	—	—	145	105	144	134
	6380.74	4.19	-1.375	25	91	79	30	85	—	48	58	40	89	82	43	70	75
	6393.60	2.43	-1.452	122	—	—	146	—	—	—	—	139	—	—	150	—	—
	6411.65	3.65	-0.596	89	—	—	105	—	—	107	—	98	—	—	112	—	140
	6419.95	4.73	-0.200	45	101	103	59	103	—	67	—	57	99	90	68	—	80
	6436.41	4.19	-2.580	—	—	—	—	—	—	15	—	—	17	—	—	—	—
	6518.37	2.83	-2.438	67	—	130	82	130	130	83	112	75	128	117	90	130	117
	6551.68	0.99	-5.790	36	—	108	—	—	—	52	94	55	—	—	61	—	107
	6574.23	0.99	-5.004	—	—	—	—	—	—	—	147	—	—	—	—	—	—
	6592.91	2.73	-1.473	—	—	—	131	—	—	141	—	—	—	—	137	—	—
	6597.56	4.80	-0.970	16	57	54	23	44	63	32	30	—	55	57	—	46	40
	6608.02	2.28	-3.930	35	—	106	51	86	115	—	64	—	102	95	64	98	81
	6609.11	2.56	-2.691	—	—	—	—	—	—	—	124	—	145	—	—	—	136
	6653.85	4.15	-2.215	—	—	—	10	29	31	—	14	—	32	—	13	24	—
	6699.14	4.59	-2.110	—	20	19	—	—	17	13	—	—	12	13	9	—	—
	6703.57	2.76	-3.060	49	118	99	63	101	108	68	82	—	104	97	72	94	91
	6704.48	4.22	-2.380	—	26	—	—	17	31	—	—	—	—	—	11	12	25
	6710.32	1.49	-4.764	50	—	—	67	122	119	74	96	70	114	111	80	109	105
	6713.74	4.80	-1.500	—	—	—	—	—	—	23	—	16	—	—	—	23	—
	6739.52	1.56	-4.794	37	113	—	—	—	115	—	—	—	—	—	—	—	97
	6745.96	4.08	-2.500	—	—	33	—	19	—	—	—	—	—	—	11	—	—
	6750.15	2.42	-2.618	81	—	—	96	—	—	92	147	—	—	149	—	—	—
	6783.70	2.59	-3.980	20	—	77	22	—	62	37	46	—	57	—	—	—	49
	6793.26	4.08	-2.326	—	—	36	13	30	—	28	—	14	—	32	—	28	—
	6810.26	4.61	-0.986	25	85	69	30	70	—	47	40	—	—	62	45	62	—
	6820.37	4.64	-1.220	—	—	58	—	—	—	—	34	—	—	—	—	—	—
	6841.34	4.61	-0.490	38	—	98	49	—	—	—	—	55	96	—	56	—	—
	6851.64	1.61	-5.320	—	77	70	—	64	71	39	42	42	75	65	—	62	—
	6858.15	4.61	-0.903	31	74	68	34	61	72	50	41	—	66	64	—	64	—
	7130.92	4.22	-0.690	59	—	130	75	127	—	—	93	—	—	122	—	117	—
	7132.99	4.08	-1.628	22	86	70	39	71	—	48	45	—	82	74	—	67	—
	Fe II	5234.62	3.22	-2.180	—	76	103	—	91	81	—	—	83	—	—	88	73
		5276.00	3.20	-1.940	65	—	—	—	—	—	—	—	—	—	—	—	—
		5284.10	2.89	-3.195	39	53	—	—	—	58	—	52	—	47	53	—	60
5325.55		3.22	-3.160	—	—	—	—	41	—	—	—	—	—	42	—	—	32
5414.07		3.22	-3.580	—	—	—	—	—	—	—	—	—	—	21	—	—	—
5425.25		3.20	-3.220	21	31	—	—	—	38	—	—	26	26	39	—	52	30
5534.84		3.25	-2.865	31	—	—	32	—	—	—	50	—	—	—	—	—	—
5991.37		3.15	-3.647	—	—	38	20	—	—	23	20	22	—	—	—	—	25
6084.10		3.20	-3.881	8	—	28	12	25	—	15	—	15	9	17	—	23	—
6149.25		3.89	-2.841	13	—	—	18	—	—	18	15	—	—	26	16	23	—
6247.56		3.89	-2.435	—	27	—	29	46	31	30	—	24	—	35	30	49	—
6416.92		3.89	-2.877	—	—	39	—	—	—	—	—	—	—	—	—	—	—
6432.68		2.89	-3.570	28	36	55	30	40	45	33	33	34	—	39	29	41	30

de Castro, D. B., Pereira, C. B., Roig, F., et al. 2016, MNRAS, 459, 4299
Dotter A., 2016, ApJS, 222, 8
Drlica-Wagner A. et al., 2015, ApJ, 813, 109
Edvardsson, B., Andersen, J., Gustafsson, B., et al. 1993, A&A, 500, 391.
Fernández-Alvar, E., Fernández-Trincado, J. G., Moreno, E., et al. 2019, MNRAS, 487, 1462
Fu, J., Kauffmann, G., Huang, M.-l., et al. 2013, MNRAS, 434, 1531
Fulbright, J. P. 2000, AJ, 120, 1841.
Fulbright, J. P. 2002, AJ, 123, 404.
Gaia Collaboration, Brown, A. G. A., Vallenari, A., et al. 2018, A&A, 616, A1

Gaia Collaboration, Prusti, T., de Bruijne, J. H. J., et al. 2016, A&A, 595, A1
Geisler, D., Smith, V. V., Wallerstein, G., Gonzalez, G., & Charbonnel, C. 2005, AJ, 129, 1428
Genovali, K., Lemasle, B., da Silva, R., et al. 2015, A&A, 580, A17
Gómez, F. A., Minchev I., O’Shea B.W et al. 2013, MNRAS, 429, 159
Gómez, F. A., White, S. D. M. Marinacci, F. et al. 2016, MNRAS, 456, 2779
Grevesse, N., & Sauval, A. J. 1999, A&A, 347, 348
Grillmair, C.J. 2006, ApJ, 645, L37
Gustafsson, B., Edvardsson, B., Eriksson, K., et al. 2008, A&A, 486, 951

TABLE 8
 NA, AL, CR AND NI LINES ANALYZED.

Element	λ	χ (eV)	log gf	Equivalent Widths (mÅ)													
				Star													
				1	2	3	4	5	6	7	8	9	10	11	12	13	14
Na I	5682.63	2.10	-0.700	36	—	—	48	—	—	—	85	86	126	—	93	130	—
Na I	5688.20	2.10	-0.400	52	—	—	59	—	—	—	92	90	133	—	94	140	—
Na I	6154.22	2.10	-1.510	9	103	98	16	84	104	42	23	53	56	86	52	57	36
Na I	6160.75	2.10	-1.210	14	121	110	25	120	112	52	38	57	77	104	64	72	56
Al I	6696.02	3.14	-1.570	14	106	88	19	86	107	59	—	50	60	88	57	63	54
Al I	6698.67	3.14	-1.870	11	67	58	—	53	75	27	—	37	43	58	36	40	33
Al I	7835.31	4.02	-0.650	—	82	66	—	58	74	39	—	46	37	63	45	41	—
Al I	8772.86	4.02	-0.170	—	—	—	25	103	117	66	—	70	62	86	66	—	—
Cr I	6330.10	0.94	-2.920	52	—	—	66	—	—	88	119	88	—	136	96	136	143
Ni I	4913.97	3.74	-0.500	—	84	—	—	103	84	—	—	—	—	78	—	—	57
Ni I	5084.10	3.68	-0.084	—	119	107	—	115	—	—	—	—	—	—	—	100	91
Ni I	5094.41	3.83	-0.998	—	—	—	—	—	—	—	30	—	—	—	—	—	—
Ni I	5115.39	3.83	-0.110	—	101	—	—	—	—	—	82	—	—	—	—	—	67
Ni I	5157.98	3.61	-1.510	11	47	34	14	—	—	—	29	—	34	47	—	24	27
Ni I	5589.36	3.90	-0.938	11	59	68	19	—	—	—	—	—	—	49	—	49	28
Ni I	5593.73	3.90	-0.682	—	72	—	—	85	78	—	35	—	—	66	—	—	40
Ni I	5748.35	1.68	-3.240	—	126	—	54	123	—	60	—	56	—	113	—	108	—
Ni I	5760.83	4.11	-0.885	8	59	50	22	56	54	28	18	21	44	51	25	37	—
Ni I	5805.22	4.17	-0.579	12	62	55	21	65	49	39	34	32	42	48	34	35	—
Ni I	5996.73	4.24	-1.037	6	29	—	6	27	—	19	—	—	—	35	19	—	—
Ni I	6053.69	4.24	-1.156	—	—	—	—	—	—	—	14	—	—	31	—	—	—
Ni I	6086.28	4.27	-0.410	16	55	62	23	67	53	36	25	35	44	—	31	48	27
Ni I	6108.12	1.68	-2.600	82	—	—	98	—	—	—	142	—	—	—	—	—	—
Ni I	6111.07	4.09	-0.865	10	52	54	19	56	—	38	—	32	44	53	34	35	—
Ni I	6128.97	1.68	-3.430	49	—	—	61	—	113	—	93	—	108	—	77	99	—
Ni I	6176.81	4.09	-0.260	32	81	78	37	80	83	53	57	49	65	78	—	91	53
Ni I	6177.24	1.83	-3.460	32	80	79	36	—	104	53	60	45	92	87	—	63	65
Ni I	6186.71	4.11	-0.880	—	—	—	—	58	—	25	26	27	—	55	—	—	—
Ni I	6204.60	4.09	-1.080	—	—	43	—	—	—	—	—	21	—	42	—	—	—
Ni I	6223.98	4.11	-0.910	14	—	54	18	44	40	27	21	23	40	39	37	—	34
Ni I	6230.09	4.11	-1.260	—	—	31	8	—	—	17	16	20	—	39	25	—	—
Ni I	6322.17	4.15	-1.115	—	30	35	9	—	—	21	14	24	25	31	23	24	—
Ni I	6378.25	4.15	-0.820	8	—	55	19	—	—	29	19	—	—	59	30	33	—
Ni I	6384.66	4.15	-1.130	—	—	—	—	—	—	21	—	—	—	—	—	—	—
Ni I	6482.80	1.94	-2.630	57	136	132	84	128	139	—	106	—	122	125	—	123	105
Ni I	6532.87	1.94	-3.350	32	99	96	44	96	—	51	63	45	86	79	—	84	73
Ni I	6586.31	1.95	-2.780	55	126	135	75	123	125	—	93	—	113	120	90	112	103
Ni I	6598.60	4.24	-0.821	—	50	36	14	38	—	26	—	22	—	38	34	37	—
Ni I	6635.12	4.42	-0.765	—	44	28	—	31	—	22	13	21	25	35	—	28	21
Ni I	6772.31	3.66	-0.797	28	87	88	46	—	—	61	53	58	72	—	63	—	73
Ni I	6842.04	3.66	-1.374	20	—	61	31	68	—	—	—	38	—	—	—	56	—

- Hanson, R. B., Sneden, C., Kraft, R. P., et al. 1998, *AJ*, 116, 1286.
- Hayden, M. R., Bovy, J., Holtzman, J. A., et al. 2015, *ApJ*, 808, 132
- Hayes C. R., Majewski, S. R., Hesselquist, S. et al., 2018, *ApJ*, 859, L8
- Heiter, U., Lind, K., Asplund, M., et al. 2015, *Phys. Scr*, 90, 054010
- Herschel, W. 1785, *Philosophical Transactions of the Royal Society of London Series I*, 75, 213
- Hunter J.D., 2007, *Computing In Science & Engineering*, 9, 90
- Ishigaki, M. N., Chiba, M., & Aoki, W. 2012, *ApJ*, 753, 64
- Iwamoto, K., Brachwitz, F., Nomoto, K., et al. 1999, *ApJS*, 125, 439
- Jones E., Oliphant T., Peterson P., et al., 2001–, *SciPy: Open source scientific tools for Python*.
- Jurić, M., Ivezić, Ž., Brooks, A., et al. 2008, *ApJ*, 673, 864
- Karakas, A. I. 2016, *Mem. Soc. Astron. Italiana*, 87, 229
- Karakas, A. I., & Lugaro, M. 2016, *ApJ*, 825, 26
- Kim, D. & H. Jerjen, 2015, *ApJ* 808, L39
- Kobayashi, C., Springel, V., & White, S. D. M. 2007, *MNRAS*, 376, 1465
- Koch, A., Grebel, E. K., Gilmore, G. F., et al. 2008, *AJ*, 135, 1580
- Koposov S.E., Belokurov V., Torrealba G., Evans N.W., 2015, *ApJ*, 805, 130
- Kurucz, R. L. 1996, *M.A.S.S., Model Atmospheres and Spectrum Synthesis*, 108, 2
- Laevens B. P. M. et al., 2015, *ApJ*, 813, 44
- Laporte, C. F. P., Gómez, F. A., Besla, G., Johnston, K. V., & Garavito-Camargo, N. 2018, *MNRAS*, 473, 1218
- Laporte, C. F. P., Johnston, K. V., Gómez, F. A. 2018, *MNRAS*, 481, 286
- Lemasle, B., François, P., Piersimoni, A., et al. 2008, *A&A*, 490, 613
- Lemasle, B., François, P., Genovali, K., et al. 2013, *A&A*, 558, A31
- Lépine, J. R. D., Cruz, P., Scarano, S., Jr., et al. 2011, *MNRAS*, 417, 698
- Lépine, J. R. D., Andrievky, S., Barros, D. A., Junqueira, T. C., & Scarano, S. 2014, *Setting the scene for Gaia and LAMOST*, 298, 86
- Letarte, B., Hill, V., Tolstoy, E., et al. 2010, *A&A*, 523, A17
- Leung, S.-C., & Nomoto, K. 2018, *ApJ*, 861, 143.
- Li T.S., Balbinot E., Mondrik N., Marshall J. L. et al., 2016, *ApJ*, 817, 135
- Li, T. S., Sheffield, A. A., Johnston, K. V., et al. 2017, *ApJ*, 844, 74
- Lind, K., Asplund, M., Barklem, P. S., & Belyaev, A. K. 2011, *A&A*, 528, A103

- López-Sánchez, Á. R., Westmeier, T., Esteban, C., & Koribalski, B. S. 2015, *MNRAS*, 450, 3381
- Luck, R. E., Gieren, W. P., Andrievsky, S. M., et al. 2003, *A&A*, 401, 939
- Luck, R. E., Andrievsky, S. M., Kovtyukh, V. V., et al. 2011, *AJ*, 142, 51
- Magrini, L., Randich, S., Kordopatis, G., et al. 2017, *A&A*, 603, A2
- Majewski, S.R., Ostheimer, J. C., Rocha-Pinto, H. J. et al., 2004, *ApJ*, 615, 738
- Majewski S.R., Skrutskie M.F., Weinberg M. D., Ostheimer J.C., 2003, *ApJ*, 599, 1082
- Majewski, S. R., Schiavon, R. P., Frinchaboy, P. M., et al. 2017, *AJ*, 154, 94
- Magrini, L., Sestito, P., Randich, S., & Galli, D. 2009, *A&A*, 494, 95
- Malhan, K., R. A. Ibata e N. F. Martin 2018, *MNRAS*, 481, 3442
- Marcon-Uchida, M. M., Matteucci, F., & Costa, R. D. D. 2010, *A&A*, 520, A35
- Martin, N. F., Ibata, R. A., & Irwin, M. 2007, *ApJ*, 668, L123
- Martin, N. F., Ibata, R. A., Rich, R. M., et al. 2014, *ApJ*, 787, 19
- Martoli, E., Teeple, D., Manset, N., et al. 2012, *Proc. SPIE*, 8451, 84512B
- McWilliam, A. 1998, *AJ*, 115, 1640
- Momany, Y., Zaggia, S., Gilmore, G., et al. 2006, *A&A*, 451, 515
- Monaco, L., Bellazzini, M., Bonifacio, P., et al. 2005, *A&A*, 441, 141
- Munari, U., Sordo, R., Castelli, F., et al. 2005, *A&A*, 442, 1127.
- Newberg, H. J., Yanny, B., Rockosi, C., et al. 2002, *ApJ*, 569, 245
- Nissen, P. E., & Schuster, W. J. 1997, *A&A*, 326, 751.
- Nordlander, T., & Lind, K. 2017, *A&A*, 607, A75
- Overbeek, J. C., Friel, E. D., & Jacobson, H. R. 2016, *ApJ*, 824, 75
- Perotoni H. D., Martin C., Newberg H. J., Rocha-Pinto H. J. et al., 2019, arXiv e-prints, arXiv:1903.08840
- Perotoni, H. D., Rocha-Pinto, H. J., Girardi, L., et al. 2018, *MNRAS*, 473, 1461
- Price-Whelan, A. M., Johnston, K. V., Sheffield, A. A., Laporte, C. F. P., & Sesar, B. 2015, *MNRAS*, 452, 676
- Prochaska, J. X., Naumov, S. O., Carney, B. W., et al. 2000, *AJ*, 120, 2513.
- Purcell, C. W., Bullock, J. S., Tollerud, E. J., Rocha, M., & Chakrabarti, S. 2011, *Nature*, 477, 301
- Ramírez, I., & Allende Prieto, C. 2011, *ApJ*, 743, 135
- Reddy, B. E., Tomkin, J., Lambert, D. L., et al. 2003, *MNRAS*, 340, 304.
- Reddy, B. E., Lambert, D. L., & Allende Prieto, C. 2006, *MNRAS*, 367, 1329
- Reddy, A. B. S., Lambert, D. L., & Giridhar, S. 2016, *MNRAS*, 463, 4366
- Rocha-Pinto, H. J., Majewski, S. R., Skrutskie, M. F., & Crane, J. D. 2003, *ApJ*, 594, L115
- Rocha-Pinto, H. J., Majewski, S. R., Skrutskie, M. F., Crane, J. D., & Patterson, R. J. 2004, *ApJ*, 615, 732
- Sales Silva, J. V., Carraro, G., Anthony-Twarog, B. J., et al. 2016, *AJ*, 151, 6
- Sbordone, L., Bonifacio, P., Buonanno, R., et al. 2007, *A&A*, 465, 815
- Sellwood, J. A., & Binney, J. J. 2002, *MNRAS*, 336, 785
- Sesar, B., Ivezić, Ž., Lupton, R. H., et al. 2007, *AJ*, 134, 2236
- Sheffield, A. A., Johnston, K. V., Majewski, S. R., et al. 2014, *ApJ*, 793, 62
- Sheffield A. A., Price-Whelan A. M., Tzanidakis A., Johnston K. V., Laporte C. F. P., Sesar B., 2018, *ApJ*, 854, 47
- Shetrone, M., Venn, K. A., Tolstoy, E., et al. 2003, *AJ*, 125, 684
- Shipp N., et al., 2018, *ApJ*, 862, 114S
- Schönrich R., Binney J., Dehnen W., 2010, *MNRAS*, 403, 1829
- Smiljanic, R., Korn, A. J., Bergemann, M., et al. 2014, *A&A*, 570, A122
- Smiljanic, R., Romano, D., Bragaglia, A., et al. 2016, *A&A*, 589, A115
- Smith, V. V., Suntzeff, N. B., Cunha, K., et al. 2000, *AJ*, 119, 1239
- Snedden, C. A. 1973, Ph.D. Thesis,
- Spina, L., Meléndez, J., Karakas, A. I., et al. 2018, *MNRAS*, 474, 2580
- Stephens, A., & Boesgaard, A. M. 2002, *AJ*, 123, 1647.
- Thielemann, F.-K., Argast, D., Brachwitz, F., et al. 2002, *Ap&SS*, 281, 25
- Thielemann, F.-K., Eichler, M., Panov, I. V., et al. 2017, *Annual Review of Nuclear and Particle Science*, 67, 253.
- Tollestrup, E. V., Pazder, J., Barrick, G., et al. 2012, *Proc. SPIE*, 8446, 84462A
- Travaglio, C., Hillebrandt, W., & Reinecke, M. 2005, *A&A*, 443, 1007
- Venn, K. A., Irwin, M., Shetrone, M. D., et al. 2004, *AJ*, 128, 1177
- Van Der Walt S., Colbert S. C., Varoquaux G., 2011, *Computing in Science & Engineering*, 13, 22
- Watkins, L. L., Evans, N. W., Belokurov, V., et al. 2009, *MNRAS*, 398, 1757
- Willman, B., Blanton, M. R., West, A. A., et al., 2005 *AJ*, 129, 269
- Wilson, J. C., Hearty, F., Skrutskie, M. F., et al. 2010, *Proc. SPIE*, 7735, 77351C
- Woosley, S. E., & Weaver, T. A. 1995, *ApJS*, 101, 181
- Worthey, G., España, A., MacArthur, L. A., & Courteau, S. 2005, *ApJ*, 631, 820
- Yong, D., Carney, B. W., & Teixeira de Almeida, M. L. 2005, *AJ*, 130, 597
- Yong, D., Carney, B. W., Teixeira de Almeida, M. L., & Pohl, B. L. 2006, *AJ*, 131, 2256
- Yong, D., Carney, B. W., & Friel, E. D. 2012, *AJ*, 144, 95
- Xu, Y., Newberg, H. J., Carlin, J. L., et al. 2015, *ApJ*, 801, 105
- Zhang, D. 2018, *Galaxies*, 6, 114